

# Global Aero-Structural Design Optimization of More Flexible Wings for Commercial Aircraft

T. F. Wunderlich \*

*German Aerospace Center (DLR), Institute of Aerodynamics and Flow Technology,  
Lilienthalplatz 7, 38108 Braunschweig, Germany*

S. Dähne †

*German Aerospace Center (DLR), Institute of Composite Structures and Adaptive Systems,  
Lilienthalplatz 7, 38108 Braunschweig, Germany*

L. Reimer ‡

*German Aerospace Center (DLR), Institute of Aerodynamics and Flow Technology,  
Lilienthalplatz 7, 38108 Braunschweig, Germany*

A. Schuster §

*German Aerospace Center (DLR), Institute of Composite Structures and Adaptive Systems,  
Lilienthalplatz 7, 38108 Braunschweig, Germany*

O. Brodersen ¶

*German Aerospace Center (DLR), Institute of Aerodynamics and Flow Technology,  
Lilienthalplatz 7, 38108 Braunschweig, Germany*

**In the scope of the DLR project VicToria (Virtual Aircraft Technology Integration Platform), an integrated process for aero-structural wing optimization based on high fidelity simulation methods is continuously developed and applied. Based upon a parametric CAD model, flight performance under transonic flight conditions and maneuver loads are computed by solving the Reynolds-averaged Navier–Stokes equations (RANS). Structural mass and elastic characteristics of the wing are determined from structural sizing of the composite wing box for essential maneuver load cases using computational structural mechanics. Static aeroelastic effects are considered in all flight conditions by direct iterative coupling between the flow solver and the structural mechanics solver. Active maneuver load alleviation (MLA) is integrated in the process by a simplified modeling of control surface deflections by using a mesh deformation technique. Landing gear and control surface integration constraints were added compared to previous versions of the optimization process.**

**Global aero-structural wing optimizations are successfully performed for wings with conventional composite wing box structure and for more flexible wings. The latter is accomplished by introducing modifications of the structural concept and the strain allowable. To reduce the  $CO_2$  emissions per passenger kilometer, the minimization of the combined fuel consumption for three typical flight missions represents the objective function. Wing optimizations are performed for variable and constant planform parameters as well as with and without consideration of MLA. A significant mass reduction of the optimized wing box is obtained with the more flexible wing concept, resulting in a drop in combined fuel consumption of about 3 %. For wing optimizations with MLA the more flexible wing concept shows an additional reduction of the combined fuel consumption in the order of 2 %. The more flexible wing concept results in optimized wing geometries with increased aspect ratio and reduced taper ratio.**

---

\*Research Scientist, Transport Aircraft, tobias.wunderlich@dlr.de

†Research Scientist, Composite Design, sascha.daehne@dlr.de

‡Research Scientist, Center for Computer Applications in Aerospace Science and Engineering, lars.reimer@dlr.de

§Research Scientist, Structural Mechanics, andreas.schuster@dlr.de

¶Vice Director, Head of Department, Transport Aircraft, o.brodersen@dlr.de

## Nomenclature

$A$	= aspect ratio
$b$	= wingspan
$C_L, C_D, C_{D,res}$	= lift coefficient, drag coefficient, residual drag coefficient
$c, c_{MAC}$	= chord, mean aerodynamic chord
$g$	= acceleration of gravity
$L/D$	= lift-to-drag ratio
$Ma$	= Mach number
$m$	= mass
$m_F, m_{F,res}$	= fuel mass, reserve fuel mass
$m_P$	= payload
$m_{TO}, m_{MTO}$	= take-off mass, maximum take-off mass
$m_W$	= wing mass
$m_F / (R m_P)$	= combined fuel consumption
$n = L / (m g)$	= load factor
$R = R_{12} + R_{23} + R_{34}$	= range (sum of mission segment ranges)
$S$	= wing area
$TSFC$	= thrust specific fuel consumption
$t$	= airfoil thickness
$t/c$	= relative airfoil thickness
$V_F$	= fuel tank volume
$x, y, z$	= coordinates
$\alpha$	= angle of attack
$\delta$	= angle of control surface deflection
$\varepsilon$	= twist angle
$\eta = 2y/b$	= relative wingspan coordinate
$\lambda$	= taper ratio
$\varphi_{LE}$	= leading edge sweep angle
Subscripts	
$CAS$	= calibrated airspeed
$cen, in, mid, out$	= center, inboard, middle, outboard wing region
$FS, MS, RS$	= front spar, middle spar, rear spar
$HTP, VTP$	= horizontal tailplane, vertical tailplane
$MG, NG$	= main gear, nose gear
$max$	= maximum value
$Ri$	= ribs
$LS$	= lower skin
$WB$	= wing fuselage configuration

## I. Introduction

The environmental impact of commercial aviation increases with the rapid growth of air travel and the  $CO_2$  share of aviation will increase due to the increase of re-newable energies in other transport sectors and in industry in general. For environmental protection and conservation of resources the main goal of the aeronautical research in Europe and in the United States of America is a strong reduction of the  $CO_2$  emissions per passenger kilometer [1–4].

To achieve this challenging goal the development timescales for new technologies have to be reduced significantly. In this context the methodologies and processes for physics based aircraft design and optimization have to be improved. Furthermore, an assessment of new technologies with consideration of all relevant disciplines and their interactions on overall aircraft level will be essential in the future.

The efficiency of commercial aircraft is determined by aerodynamic performance in terms of lift to drag ratio, aircraft empty mass, and thrust specific fuel consumption of the engine. For the accurate drag prediction under cruise flight conditions the flow physics of transonic and turbulent flow can be taken into account by using RANS-based

computational fluid dynamics (CFD). To reduce the structural mass composite materials like carbon fiber reinforced polymers (CFRP) have been introduced in aircraft manufacturing. The corresponding structural concepts and sizing criteria have to be considered in the structural analysis and sizing process by using structural mechanics solvers based on the finite element method (FEM).

Within the aero-structural wing optimization the optimum trade-off between the aerodynamic performance and the wing mass is achieved through combining high fidelity methods for numerical flow simulation of the aircraft outer shape and structural sizing of the wing box with an appropriate optimization algorithm. Thereby, the interaction of aerodynamic forces and wing deformations have to be considered for accurate flight performance and static maneuver loads prediction by using fluid-structure coupling.

Wing design and optimization is a multidisciplinary task with a lot of practical constraints. For example, the size of the tail has to fulfill all stability and control constraints and thus depends on center of gravity range and wing geometry. Furthermore, the landing gear integration and the space allocation for the control surfaces including their actuators have to be considered. Neglecting the landing gear integration leads to unrealistic optimization results as shown in [5].

With increasing knowledge of composite materials further mass reduction potentials can be exploited by better adaptation of fiber direction to internal loads, introduction of advanced structural concepts, and new manufacturing processes. The more flexible wing concept is a result of mass reduction due to new structural concepts with increased strain allowable and applied to the current generation of aircraft from Boeing (Boeing 787 and Boeing 777-8/9). In addition the passive load alleviation due to static aeroelastic effects leads to further wing mass reduction.

The technology of active maneuver load alleviation (MLA) reduces the wing bending moment by using trailing edge control surface deflections to adapt the lift distribution under maneuver flight conditions. This technology has been published by White [6] for example and successfully applied to the Lockheed L-1011 [7]. In modern airliners, the maneuver load alleviation functions are an integral part of the flight control system. The active and passive load alleviation technologies have to be integrated into the sizing process of the aircraft structure and result in longer maintenance intervals and mass reductions. The earlier load alleviation is considered in aircraft design process, the greater is the benefit from snowball effects. Therefore, a physical modeling of active maneuver load alleviation technology is pursued in preliminary aircraft design.

Improvements in automation and coupling of accurate simulation methods in combination with advances in numerical optimization strategies lead to the emergence of multidisciplinary design optimization (MDO) based on high fidelity methods. The challenge in using MDO based on high fidelity methods is the large number of design parameters and the increased computing effort. To overcome this issue, the adjoint method enables the efficient calculation of the flow variable gradients as a function of the design parameters for gradient based optimization [8, 9]. Up-to-date applications of the adjoint approach for multidisciplinary wing optimization have been shown in the publications of Kenway and Martins [5]; Liem, Kenway, and Martins [10]; and Keye et al. [11]. These publications show that the gradient based optimization using the adjoint approach is an adequate method for multidisciplinary wing optimization with high fidelity simulation programs and a large number of design parameters.

In this work an alternative MDO approach is introduced for cases in which gradients cannot be computed efficiently for all relevant disciplines. This applies particularly to cases which involve CAD modeling and structural sizing of composite structures using proprietary codes. Additionally, the gradients based approaches have to be reconsidered for flows near the maximum lift including flow separations and the usage of active control surface deflections. Furthermore, a certain degree of flexibility in the process architecture and optimization strategy is desired. Especially the option to use optimization strategies seeking for the global optimum is important.

## II. MDO architecture and process chain

In the DLR project VicToria [12–14], an integrated process for aero-structural wing optimization based on high fidelity simulation methods is continuously developed and improved. A detailed description of the original process chain and their successful application is published by Wunderlich et al. [15, 16]. The improvements relate to the introduction of grid deformation techniques for large geometry changes and simplified control surface deflections. Further extensions include a landing gear integration, a tail sizing based on handbook methods and a trim drag estimation functionality. The integrated process chain can be characterized by the following items:

- Usage of a central file format for parametric aircraft description,
- Tail sizing and landing gear integration,
- Automated grid deformation for aerodynamic simulation,
- Automated structural model generation for structural simulation,

- Parallel static aeroelastic analysis for an arbitrary number of flight conditions,
- Structural wing box sizing for composite structures,
- Simplified control surface deflections based on grid deformation, and
- Large geometry changes for usage of global optimization strategy.

### A. MDO architecture

The MDO architecture of the integrated process chain falls in the category of MDF optimizations (Multi-Disciplinary Feasible) and can be described as ASO (Asymmetric Subspace Optimization) according to Martins and Lambe [17]. In the MDF architecture a full MDA (multidisciplinary analysis) is performed for each optimization iteration. This means that the investigated design fulfills all constraints in each optimization step and hence is called a feasible design.

### B. Process chain description

The process chain applied is illustrated in terms of XDASM-diagrams (Extended Design Structure Matrix) [18]. This type of diagram combines information on process flow and data dependencies. Each component in the diagram receives input data in vertical direction and provides output data in horizontal direction. Input and output data are marked by parallelograms. Thick gray lines show the data flow, and thin black arrows indicate the process flow. The numbering system defines the order in which the components are executed.

In Fig. 1, the connection between the aero-structural wing analysis process chain and optimizer is shown. The optimizer controls the values of the design parameters based on the value of the objective function.

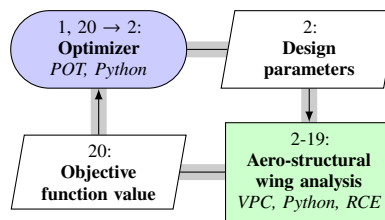


**Fig. 1 Connection between aero-structural wing analysis process chain and optimizer.**

The flow chart of the process chain for aero-structural wing analysis is shown in Fig.2. In every optimization step, the geometrical aircraft description of the baseline configuration is recalculated and updated in accordance with the current values of the design parameters. The resulting aircraft geometry is transferred to the subsequent simulation programs by using the central data format CPACS. In the Common Parametric Aircraft Configuration Schema (CPACS) [19, 20], the aircraft data are organized hierarchically and stored in the human readable common Extensible Markup Language (XML). The recalculation of the aircraft geometry includes the wing positioning relative to the fuselage, the integration of the main landing gear, the sizing of the tail, and the check of geometrical constraints. If the landing gear integration ended successfully and all geometrical constraints are fulfilled, the process will automatically continue. Otherwise, the process terminates and the optimizer starts another run with a new set of design parameter values. This approach ensures, that time consuming aero-structural wing analyses are only performed for wing geometries that fulfill all geometrical constraints.

In the setup and preparation stage of the optimization, a parametric CAD model has been built automatically in CATIA® V5. The automated CAD model generation process uses the geometry description of the reference aircraft configuration in CPACS as input and generates a parametric CAD model with the same parameterization and topology. The main function of the CAD system is to provide the surfaces and intersections computed from the wireframe geometry description in CPACS. In Fig. 3, the resulting wireframe model for the geometry of the reference aircraft configuration is shown. The model consists of fuselage sections, belly fairing sections, wing sections, and corresponding guide curves for the description of the geometry between the sections. In addition, the CAD model generation process includes the construction of auxiliary geometry for the automated aerodynamic surface mesh generation.

For automatic surface mesh generation, the commercial software Pointwise® is applied by using a control script written in the Glyph scripting language. Glyph is an extension to the Tcl programming language that allows access to all Pointwise® commands and entities. The control script is generated as part of the automated CAD model generation process. Within this CAD model generation process all geometry elements are named uniquely and the corresponding

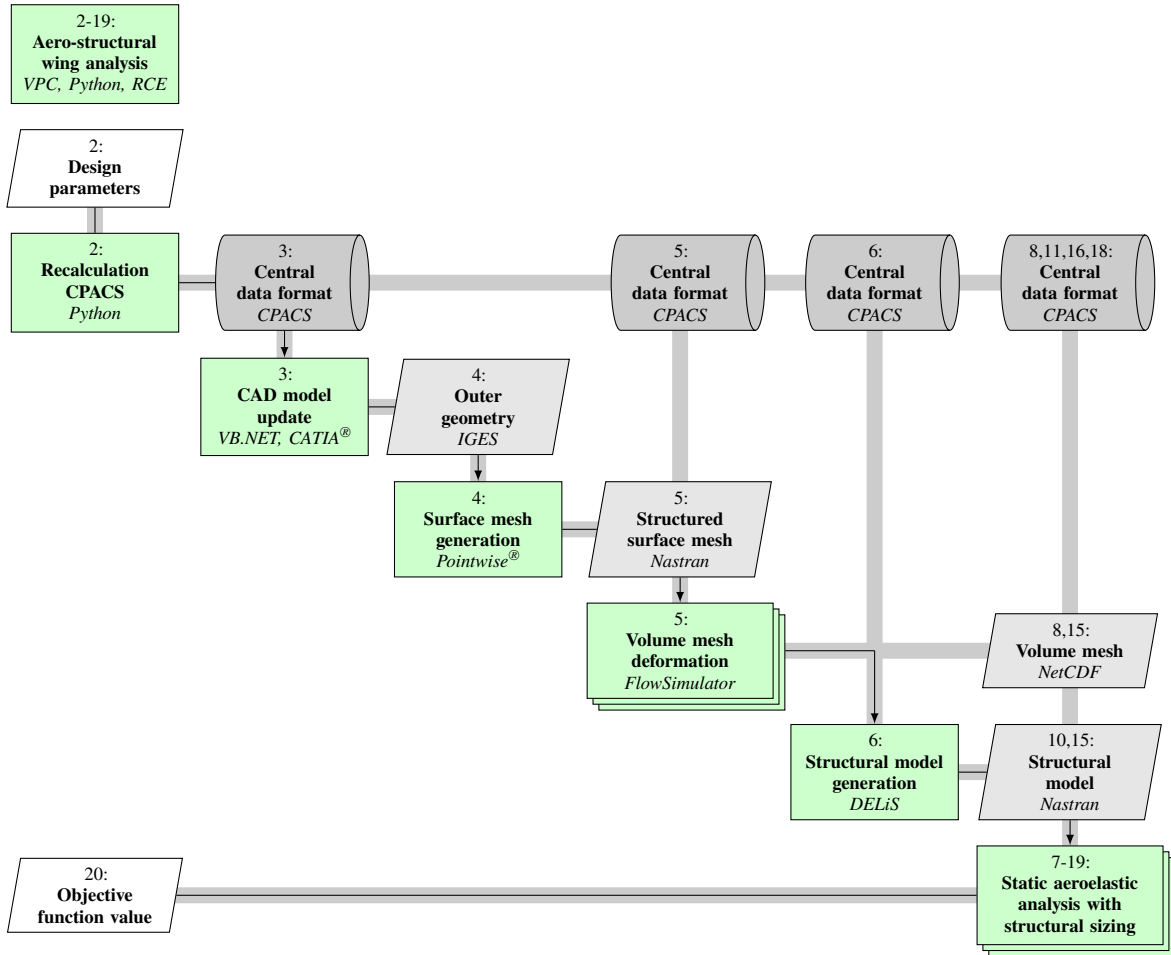


Fig. 2 Flow chart of the process chain for aero-structural wing analysis.

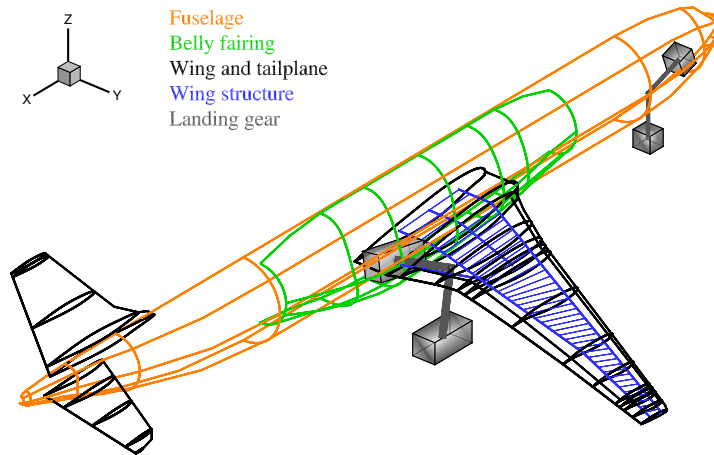


Fig. 3 Wireframe model of the reference aircraft geometry based on CPACS.

lines for surface mesh generation in Pointwise<sup>®</sup> are written automatically to the control script. The data transfer between the CAD model and the surface mesh generation is realized by using the Initial Graphics Exchange Specification (IGES) format.

Within the CFD volume mesh deformation process, the mesh representing the baseline configuration is deformed in two steps for all flight conditions in parallel. In the first step, the geometrical changes between the baseline and the current geometry are computed based on the corresponding structured multi-block (SMB) surface meshes. The latter result from the surface mesh generation and have an identical mesh topology with the same number of points. In the second step, the control surface deflections are taken into account. Corresponding to the control surface deflection to be produced, the surface mesh displacement field is computed for each flight condition. It is propagated to the CFD volume mesh by using the Elasticity Analogy (EA) mesh deformation method [21] available in the FlowSimulator [22–24] environment.

For the generation of the structural model the DLR in-house tool DELiS (Design Environment for thin-walled Lightweight Structures) [25] is used. Based on the central data format CPACS, DELiS automatically creates an initial wing geometry with means of the DLR-tool TIGL [26]. A consistent finite element mesh is then generated using the open-source tool Gmsh [27]. The finite element model is made up of shells elements enriched with physical properties of the wing spars, ribs, and skin cells and finally exported for the commercial FE solver MSC Nastran<sup>™</sup>.

The flow chart of the parallel static aeroelastic analysis process with structural sizing is shown in Fig.4. The fluid-structure coupling loop is marked in yellow. It stops when the values for the lift-to-drag ratio of the design mission, the wing mass and the objective function value are converged. The corresponding convergence criteria are summarized in Tab. 1. The fluid-structure interaction belongs to the category of loosely coupled analysis [28, 29], with the main difference of replacing the structural analysis of a sized wing structure by a combined structural wing analysis and sizing process. The integration of the structural sizing process into the fluid-structure coupling loop reduces the number of iterations by introducing a damper like behavior.

For all flight conditions defined in the central data format CPACS, aerodynamic forces and coefficients are computed using RANS-based CFD simulations. The flow simulations are performed by using the DLR TAU-Code [30, 31] which is integrated in the HPC framework FlowSimulator [22]. The solver’s capabilities with respect to accurate flow predictions, also in near off-design regions, have been demonstrated in numerous publications, including those of the AIAA Drag Prediction Workshop Series [32]. The approach ensures that flight performance under cruise flight conditions and selected maneuver loads with consideration of flow separations are analyzed accurately and efficiently.

		Convergence criterion
Lift-to-drag ratio design mission	$L/D$	$\frac{\Delta(L/D)}{L/D} \leq 0.001$
Wing mass	$m_W$	$\frac{\Delta m_W}{m_W} \leq 0.005$
Combined fuel consumption	$m_F/(R m_P)$	$\frac{\Delta(m_F/(R m_P))}{m_F/(R m_P)} \leq 0.002$

**Table 1 Convergence criteria of the fluid-structure coupling loop.**

Based on the aerodynamic loads computed for the flight conditions considered, the wing-box structure is sized. Within the structural analysis and sizing process, the latter forms an inner loop. For a fixed aerodynamic load, the objective is to fulfill the structural constraints in terms of failure criteria and converge the margins of safety (MoS) and wing mass. The main results of the process are the wing mass and the deformed wing shapes for the flight conditions considered. The structural analysis and sizing process uses the commercial software MSC Nastran<sup>™</sup> for computing the internal loads and stresses. The commercial software HyperSizer<sup>®</sup> is applied for sizing the composite wing box.

In Fig. 5, the flow chart of the iterative structural sizing and analysis process is shown. For given structural model and aerodynamic forces, internal loads are computed for all flight conditions at once. Element thicknesses and resulting structural wing mass are computed iteratively in the course of the structural sizing and optimization process. Based on the resulting element thicknesses the structural model is updated and the structural sizing loop continues until the wing mass reaches convergence. Finally, for the flight conditions considered, structural analyses for the sized structural model are performed.

The structural deformations form the input for the CFD volume mesh deformation as shown in Fig 4. The mesh deformation method based on radial basis functions (RBF) [33] available in the FlowSimulator is used. Afterwards, the objective function is evaluated and the convergence criteria of the static aeroelastic analysis are examined. In order

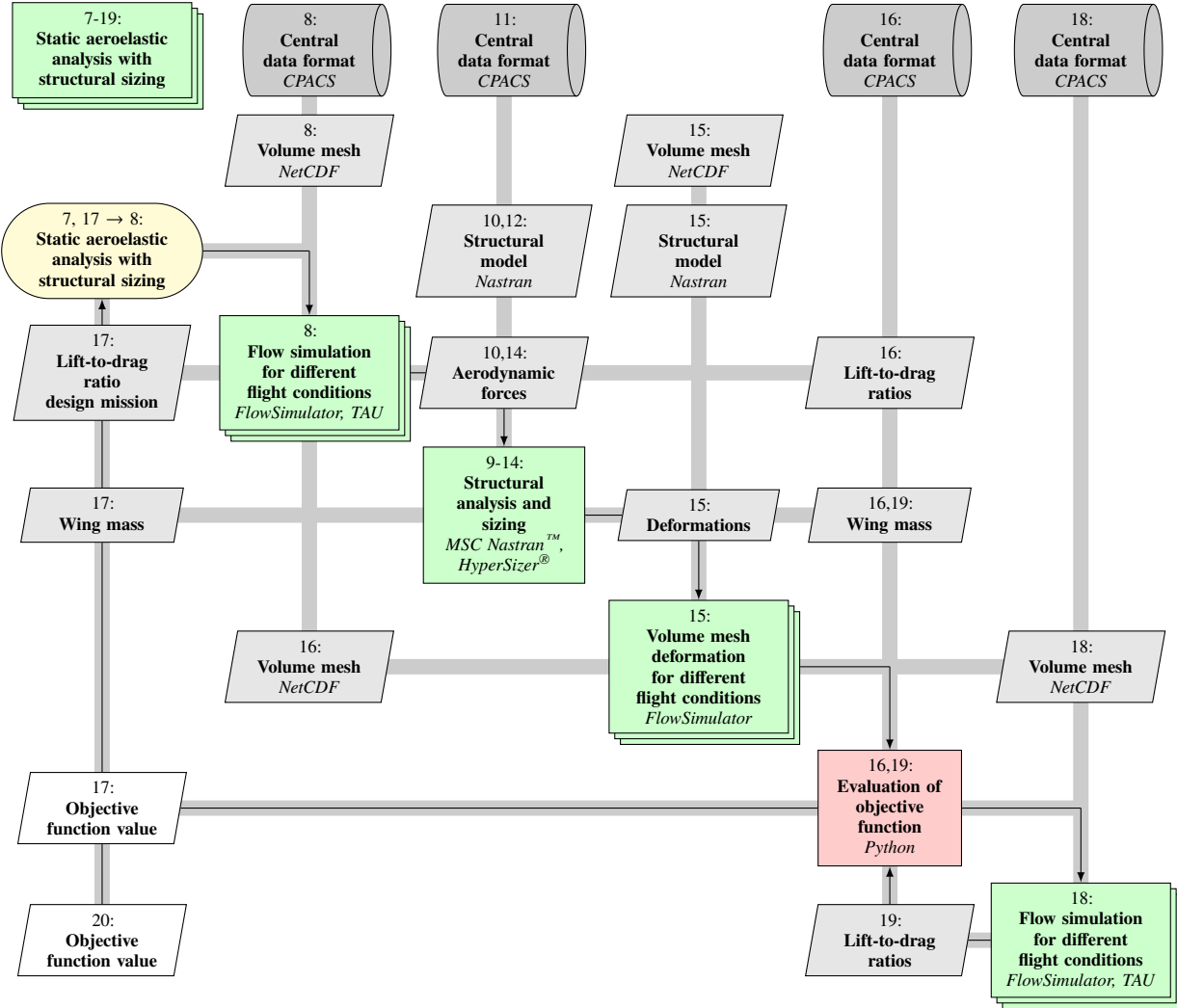


**Fig. 4 Flow chart of the parallel static aeroelastic analysis with structural sizing.**

to reduce the overall computing time, the convergence thresholds applied in CFD simulation and structural analysis and sizing process are reduced with the growing number of fluid-structure coupling iterations. Once convergence of the fluid-structure coupling loop is reached, a final CFD computation is performed in which the CFD solver's convergence threshold is further decreased to increase the accuracy of the flight performance prediction, especially regarding the lift-to-drag ratio. The last step in the process chain is the recalculation of the objective function value for the multidisciplinary assessment of the wing design. As shown in Fig. 1 the optimization algorithm then calculates a new set of values for the design parameters based on the value of the objective function. After the optimization run has finished the optimized vector of design parameters represents the main result of the process chain for the corresponding optimization problem.

### C. Global optimization strategy

For the wing optimizations a surrogate based optimization (SBO) method [34] has been selected. This global optimization strategy represents an adequate compromise between exploring the design space and locating the optimum. The selected optimization method is an implementation of the optimization method EGO (Efficient Global Optimizer), which has been introduced by Jones et al. [35] and is discussed in Forrester et al. [36]. At the beginning of the optimization a design of experiments (DoE) for a selected number of samples is performed. For the calculated objective function value and for each selected constraint a surrogate model based on kriging [37] is built. These surrogate models

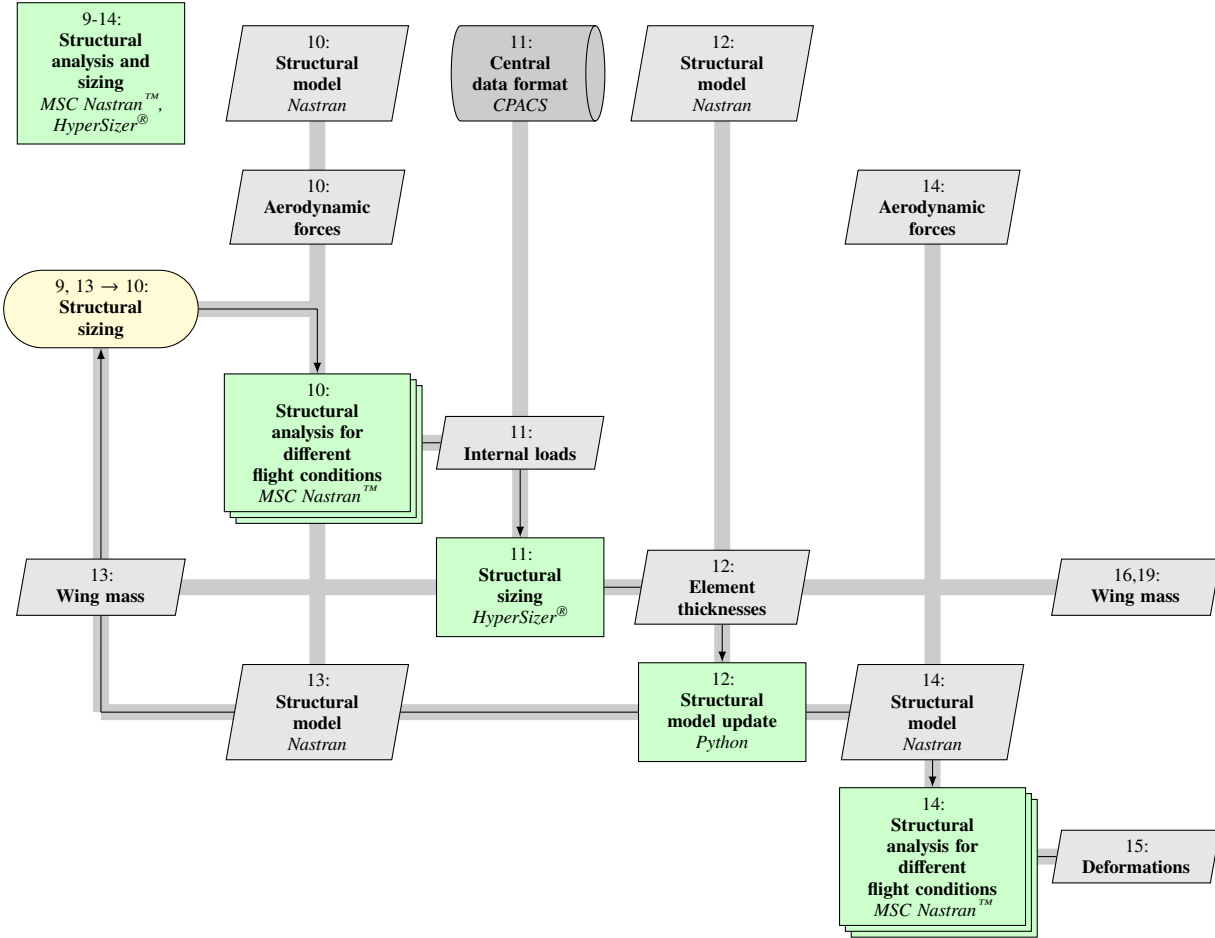


**Fig. 5 Flow chart of the combined structural analysis and sizing process.**

are able to model the nonlinear behavior of the objective and constraints. Additionally, a statistical error estimation is included. Based on the surrogate models of the objective function and constraints, a hybrid optimization strategy is used to find the optimum in terms of expected improvement (EI), which combines the predictions of objective function value and model error. The hybrid optimization strategy starts with a global optimization method and the localization of the optimum is improved by the application of a local optimization method. For the resulting global optimum in terms of expected improvement a recalculation with the physical model is performed. The result of this recalculation is then used to improve the surrogate models for the objective function value and constraints. The described optimization procedure is iterated until convergence is reached.

### III. More flexible wing

For the quantitative assessment of more flexible wings the structural concept and strain allowable have to be defined for the conventional and the more flexible wing box structure. Then a wing design optimization with the same objective, design parameters, and constraints has to be performed for both wing box structures. The comparison of the optimized wings in terms of cruise flight performance and wing mass allows the quantification of potential reduction of  $CO_2$  emissions per passenger kilometer.

For the more flexible wing the structural concept and the maximum strain allowable have been changed. The structural concept of the conventional composite wing structure consists of classical upper skin ply share and blade stringers. For the strain allowable a conservative value of  $3500 \mu\text{m}/\text{m}$  has been selected as proposed in Military Handbook [38]. Through a detailed consideration of stringer constraints and stiffness, the evaluation of a more flexible wing becomes possible, while relevant structural constraints are considered. For stiffened composite panels the more

flexible wing concept has been investigated by Bach and Hühne [39].

In this work, the more flexible wing has been modeled with a stringer dominant structural concept of the upper cover. This includes a selected upper skin percentage ply share of (10/80/10) and the usage of I-stringers. Based on the modified structural concept a value of 5000  $\mu\text{m}/\text{m}$  has been selected for the strain allowable of the more flexible wing. The percentage ply share of the lower skin, spars, and ribs has been considered in one of the aero-structural wing optimizations. In Table 2 the differences between the structural concepts of the conventional composite wing and the more flexible wing have been summarized.

		Structural concept of conventional composite wing	Structural concept of more flexible wing
Structural concept of the upper covers		Skin dominated design	Stringer dominated design
Stringer type		Blade stringer	I-stringer
Strain allowable	$\epsilon$	3500 $\mu\text{m}/\text{m}$	5000 $\mu\text{m}/\text{m}$
Upper skin percentage ply share center wing box	$0^\circ / \pm 45^\circ / 90^\circ$	70/20/10	10/80/10
Upper skin percentage ply share inboard	$0^\circ / \pm 45^\circ / 90^\circ$	60/30/10	10/80/10
Upper skin percentage ply share mid wing	$0^\circ / \pm 45^\circ / 90^\circ$	60/30/10	10/80/10
Upper skin percentage ply share outboard	$0^\circ / \pm 45^\circ / 90^\circ$	40/50/10	10/80/10

**Table 2 Structural concept overview.**

#### IV. Multi-mission aero-structural wing optimizations

In the DLR project VicToria multi-mission aero-structural wing optimizations have been successfully applied to optimize wing planform, twist, and thickness distribution of the Airbus XRF1 research configuration. To investigate the more flexible wing concept, the optimizations have been performed for a conventional composite wing structure and for a more flexible composite wing structure. Thereby, the XRF1 is an Airbus provided industrial standard multi-disciplinary research testcase representing a typical configuration for a long range wide body aircraft.

In the first step, the wing optimizations with a conventional composite wing structure have been performed. The result of the twist and thickness distribution optimization represents the baseline. With the optimization of wing planform, twist, and thickness distribution, the design space has been further extended and shows the full potential of multidisciplinary wing optimization with the introduced optimization approach. Additionally, a result for the optimization of wing planform, twist, and thickness distribution with consideration of maneuver load alleviation by using active control surface deflections is presented.

In the next step the more flexible wing has been introduced by changing the structural concept and the maximum strain allowable. For the baseline with a more flexible wing, the composite layer distribution of the skins, spars, and ribs and the twist and thickness distribution have been optimized. The resulting composite layer distribution has been transferred to the other more flexible wing optimizations. In these more flexible wing optimizations the wing planform, twist, and thickness distribution have been optimized for fixed composite layer distribution with and without the consideration of active maneuver load alleviation, respectively.

##### A. Design task with objective and constraints

The design task describes the objective function, the design space, and the constraints. In this work the wing design for a long range commercial aircraft configuration has been selected. The objective function is based on flight physics and economic aspects have been neglected. To achieve more realistic results the tail sizing and geometrical constraints for landing gear integration have been considered in the wing design.

###### 1. Flight envelope and load cases

For the structural sizing of the wing box the maneuver load cases with the maximum loads have to be defined. These maneuver load cases have been derived from the flight envelope limits, which are summarized in Tab. 3. The flight envelope limits of the Airbus XRF1 research testcase have not been published and therefore the values have been transferred from the similar Airbus A330-200 [40]. The positive and negative limit of the maneuvering load factor

result from the certification regulations CS-25/FAR 25. Based on the flight envelope limits the maneuver load cases have been selected. In Tab. 4 an overview of the selected maneuver load cases is given.

Maximum altitude	$H_{max}$	FL 410 (12 500 m)
Maximum operating Mach number	$Ma_{MO}$	0.86
Maximum operating limit speed	$V_{MO,CAS}$	330 kn (170 m/s)
Design diving Mach number	$Ma_D$	0.93
Design diving speed	$V_{D,CAS}$	365 kn (188 m/s)
Positive and negative limit maneuvering load factor	$n$	+2.5/ - 1.0

**Table 3 Flight envelope limits.**

For positive limit load factors the upper cover of the wing box is loaded in general with tensile stress and the lower cover with compression stress. In the case of negative limit load factors the loading with tensile stress and compression stress is reversed in the wing box covers. Due to different failure mechanism for tensile and compression stress of lightweight structures and the corresponding differences in the sizing criteria, the selection of load cases includes load cases with the positive and the negative limit maneuvering load factor.

For the pull up maneuver the combination of maximum takeoff mass and positive limit maneuvering load factor has been selected. The push over maneuver is defined for the combination of maximum takeoff mass and negative limit maneuvering load factor. Additionally, a steady state load case with maximum aileron deflection and two thirds of the maximum positive load factor has been selected to represent the aerodynamic loads at the beginning of a roll maneuver. With this load case, a high level of wing torsional loads is considered in the structural wing box sizing.

		Pull up maneuver	Push over maneuver	Roll maneuver
Altitude	$H$	0 m	6096 m	0 m
Mach number	$Ma$	0.552	0.784	0.552
Lift coefficient wing fuselage	$C_{L,WB}$	0.739	-0.319	0.493
Load factor	$n$	2.5	-1.0	1.667

**Table 4 Load cases for structural sizing.**

## 2. Flight missions and objective function

The objective function of the multi-mission aero-structural wing optimizations is the combined fuel consumption of three selected flight missions. In this work, the fuel consumption is defined in terms of fuel burn per range and payload. Hence, the combined fuel consumption is the weighted sum of the corresponding mission fuel consumption as given in Eq. (1).

$$\frac{m_F}{R m_P} = \sum_i w_i \left( \frac{m_F}{R m_P} \right)_i \quad (1)$$

In Table 5 an overview of the selected flight missions and weight factors is shown. With the selected weighting factors the expected relative frequency of the missions in operation has been considered.

For the study and design mission the design Mach number of the Airbus XRF1 has been selected. The design mission range is set to 6500 nm and the corresponding payload is a result of the aero-structural wing analysis. The selection of range and payload for the study mission is based on a typical long range mission with a load factor of 0.85 and represents the mission for which the aircraft will be optimized primarily. The difference between the study mission is the increased cruise Mach number to consider off-design conditions in the wing optimization.

To compute the fuel consumption of each flight mission a modeling from conceptual design [41, 42] has been used. Thereby, the flight mission has been divided into five segments and the corresponding aircraft mass fractions for take-off, climb, descend, and landing have been transferred from typical values given in the textbook published by Jenkinson [43] to the reference aircraft configuration Airbus XRF1. The flight mission segments are summarized in Table 6.

		Study mission	High speed mission	Design mission
Weight factor	$w_i$	0.6	0.1	0.3
Cruise Mach number	$Ma$	0.83	0.85	0.83
Range	$R = R_{12} + R_{23} + R_{34}$	4000 nm (7408 km)	4000 nm (7408 km)	6500 nm (12 038 km)
Payload	$m_P$	40 800 kg	40 800 kg	-
Reserve fuel ratio	$m_{F,res}/m_F$	0.1410	0.1410	0.0950

**Table 5 Flight missions for flight performance prediction.**

Segment number	Mission segment	Aircraft mass fraction	Reference
1	Taxi and take-off	$m_1/m_{TO} = 0.997$	[43]
2	Climb and accelerate	$m_2/m_1 = 0.981$	[43]
3	Cruise	$m_3/m_2 = \exp\left(-\frac{(C_1+C_2 Ma) R_{23}}{\sqrt{\kappa R \theta_{SL}} Ma L/D}\right)$	Eq. (3)
4	Descent for landing	$m_4/m_3 = 0.998$	[43]
5	Landing and tax	$m_5/m_4 = 0.997$	[43]

**Table 6 Flight mission segments.**

For the cruise segment of the flight mission a constant Mach number and constant lift-to-drag ratio have been assumed. Furthermore, the thrust specific fuel consumption has been modeled by a formula published by Mattingly [44]. This formula describes the dependency of the thrust specific fuel consumption from the flight conditions for a given engine and has been adapted to a typical engine map in the Rolls-Royce Trent 1000 class. The formula with the adopted parameters are given in Eq. (2).

$$TSFC = \frac{C_1 + C_2 Ma}{g} \sqrt{\frac{\theta}{\theta_{SL}}} \quad \text{with } C_1 = 0.245 \text{ h}^{-1} \text{ and } C_2 = 0.415 \text{ h}^{-1} \quad (2)$$

The aircraft mass fraction for the cruise segment is calculated with Eq. (3), which has been derived from the well-known Breguet range equation and the thrust specific fuel consumption in Eq. (2).

$$R_{23} = \underbrace{\sqrt{\kappa R \theta_{SL}}}_{\text{const.}} \frac{Ma}{C_1 + C_2 Ma} \frac{L}{D} \ln \frac{m_2}{m_3} \quad \text{with } \kappa = 1.4, R = 287.05 \text{ m}^2/(\text{s}^2 \text{ K}) \text{ and } \theta_{SL} = 288.15 \text{ K} \quad (3)$$

For each flight mission the corresponding lift-to-drag ratio for the cruise segment is a result of the aerodynamic coefficients of the flow simulation for the wing body configuration, the estimated aerodynamic coefficients of the tail, and the given residual drag coefficient as shown in Eq. (4).

$$\frac{L}{D} = \frac{C_L}{C_D} = \frac{\overbrace{C_{L,WB} + C_{L,HTP}}^{\text{flow simulation}}}{\underbrace{C_{D,WB} + C_{D,HTP} + C_{D,VTP}}_{\text{flow simulation}} + \underbrace{C_{D,res}}_{\text{const.}}} \quad (4)$$

The lift coefficient of the horizontal tail is a result of aircraft trimming for the prescribed center of gravity position. This aircraft trimming loop based on the equilibrium of forces and moments around the center of gravity is not described in detail here. For the drag coefficient prediction of the tail a simplified approach from conceptual design [45] based on Prandtl lifting-line theory and flat plate analogy has been used.

The take-off mass of the aircraft is the sum of the residual mass  $m_{Res}$  (structural mass without the wing and tail including the operating items mass), the wing mass  $m_W$ , the tail mass, the payload, and the fuel masses (mission and reserve fuel) as shown in Eq. (5).

$$m_{TO} = \overbrace{m_{Res} + m_W + m_{HTP} + m_{VTP}}^{\text{operating empty mass } m_{OE}} + m_P + m_F + m_{F,res} \quad (5)$$

The wing mass is a result of the structural sizing of the wing box and the tail mass is estimated by scaling the tail mass of the reference aircraft with the tail surface ratio after tail sizing. Thereby, the tail sizing based on conceptual design methods by using constant tail volume coefficients [42]. The fuel mass follows directly from the aircraft mass difference for the complete flight mission as shown in Eq. (6).

$$m_F = m_{TO} - m_5 \quad (6)$$

For the calculation of the fuel consumption the required equations are listed in Table 7. Thereby, the fuel mass ratio  $m_F/m_{TO}$  is computed from the aircraft mass fractions with the given range  $R$  and the lift-to-drag ratio  $L/D$  for the cruise segment. For the study mission and the high speed mission the payload is specified and the take-off mass has to be calculated. In the design mission the take-off mass equals the maximum take-off mass and the payload is resulting from the cruise flight performance and wing mass. For both cases the corresponding equations are evaluated in terms of the payload ratio  $m_P/m_{TO}$ . With the fuel mass ratio and the payload ratio the fuel consumption per range and payload follows directly from the last equation in Table 7.

Fuel mass ratio	$\frac{m_F}{m_{TO}} = 1 - \frac{m_1}{m_0} \frac{m_2}{m_1} \frac{m_3}{m_2} \frac{m_4}{m_3} \frac{m_5}{m_4}$
	$\frac{m_P}{m_{TO}} = 1 - \frac{m_{OE}}{m_{TO}} - \left(1 + \frac{m_{F,res}}{m_F}\right) \frac{m_F}{m_{TO}}$ for specified $m_{TO}$ and variable $m_P$
Payload ratio	$\frac{m_P}{m_{TO}} = \frac{1 - \left(1 + \frac{m_{F,res}}{m_F}\right) \frac{m_F}{m_{TO}}}{m_{OE} + m_P} m_P$ for specified $m_P$ and variable $m_{TO}$
Fuel consumption	$\frac{m_F}{R m_P} = \frac{m_F}{m_{TO}} \frac{m_{TO}}{m_P} \frac{1}{R_{12} + R_{23} + R_{34}}$

**Table 7 Used formulas for the computation of the fuel consumption.**

### 3. Design parameters and constraints

The outer shape of the wing has been parameterized with the design parameters shown in Fig. 6. Thereby, the wing planform is calculated from wing area, aspect ratio, leading edge sweep angle, and the taper ratios of the inboard, mid wing, and outboard wing region. Furthermore, the twist and relative thickness distribution are defined in the corresponding wing sections. In the wing sections between these sections the values of the twist and relative thickness are interpolated linearly. The fuselage shape has been held constant during the wing optimizations. For the belly fairing an adaptation to the root section of the wing has been considered by scaling the middle section of the belly fairing in the x-direction while keeping the relative x-position constant. The positioning of the wing in the x-direction has been performed by maintaining the x-position of the aerodynamic center. The z-position of the wing root section has been kept constant.

The wing box regions and the global wing box design parameters are shown in Fig. 7. Thereby, the wing box has been separated into four regions. The definition of the spars is based on the relative positioning of spar points, which are given in relative span and relative chord coordinates. For the definition of the front spar only three spar points are used. The spar geometry is planar between these spar points. The rear spar is defined with four spar points as shown in Fig. 7. Between the middle wing region and the outboard wing region a small kink exists in the definition of the rear spar. The relative chord position of the inner rear spar point has been used as a design parameter in the wing planform optimizations. The position of the middle spar is calculated as a function of the front and rear spar positions. For the ribs a constant rib spacing has been considered. In the center wing and inboard region the ribs are oriented in flight direction and in the middle and outboard wing region the ribs are positioned normal to the front spar. These rib orientations are typical for Airbus aircraft. For the structural optimization of the wing box the percentage ply share of the lower skin, spars, and ribs have been defined as global design parameters in the four selected wing regions. The corresponding design parameters are shown in Fig. 7. In Table 8 all selected global design parameters are summarized.

The definition of the control surfaces and the fuel tanks are shown in Fig. 8. For the consideration of the active maneuver load alleviation the deflections of the inboard flap, outboard flap and outboard aileron have been used as global design parameters in the corresponding wing optimizations.

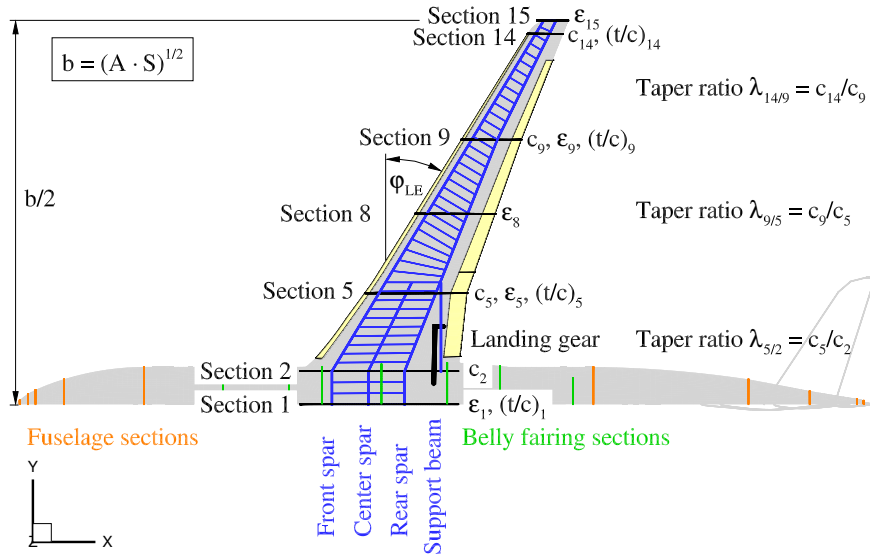


**Fig. 6 Fuselage and wing sections and the definition of outer shape design parameters.**

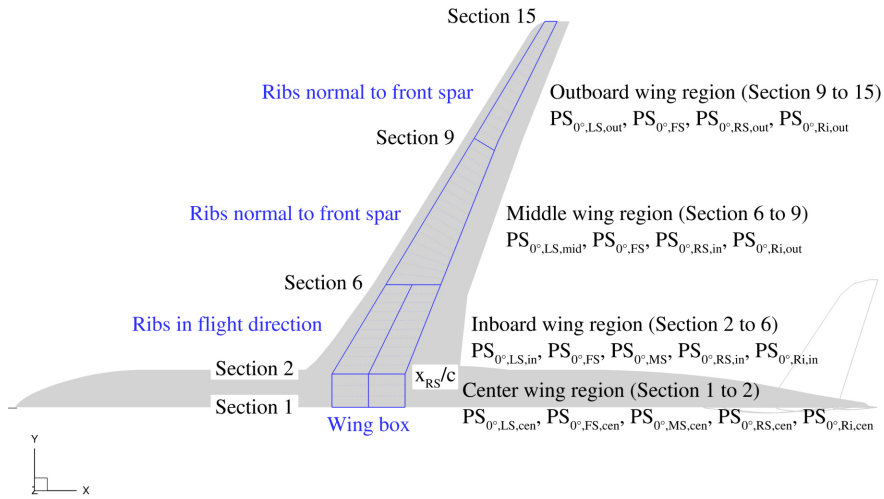


**Fig. 7 Wing box regions and the definition of global wing box design parameters.**

The fuel tank volume is computed based on the fuel tanks definition in Fig. 8 and a usable volume factor of 0.85 for integral wing tanks [42]. During the wing optimization the required fuel tank volume is calculated for all selected flight missions and compared with the useable fuel tank volume. The fuel tank volume constraint has been considered in all wing optimizations.

With the consideration of geometry constraints for the integration of a landing gear and the control surfaces, a better comparability of the optimization results with the baseline aircraft configuration is achieved. Figure 9 gives an overview of the geometrical constraints, which have to be fulfilled for each wing design. This includes the positioning of the main gear wheel on the ground with a given relative x-position while maintaining the minimal allowed distances between the main landing gear, the control surfaces, and the wing box.

The landing gear static load at ground conditions is a result of current aircraft mass and the corresponding static

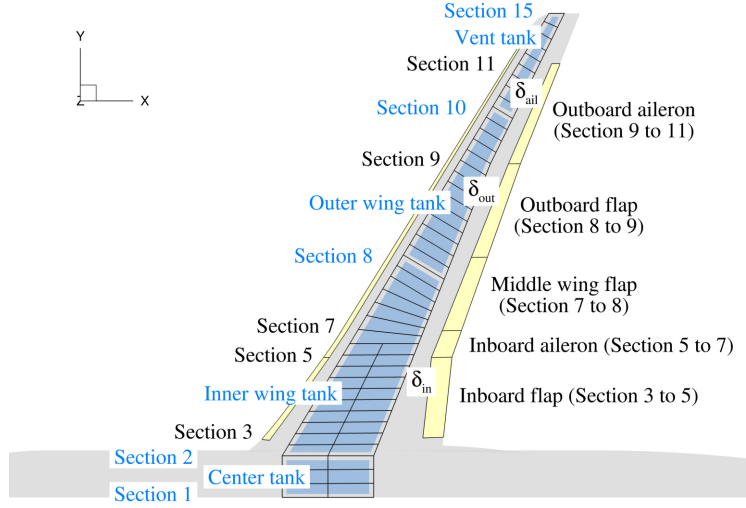


**Fig. 8** Definition of control surfaces and fuel tanks.

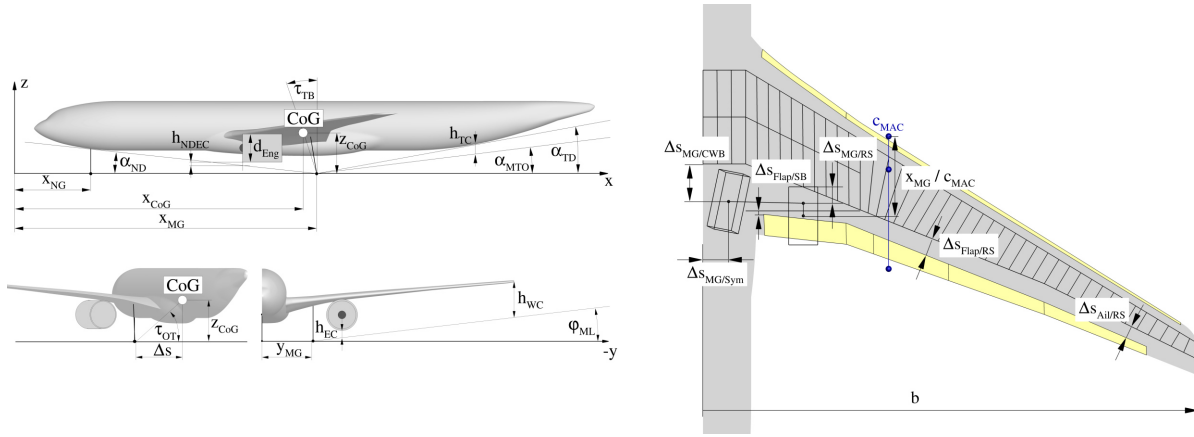


**Fig. 9** Geometrical constraints.

load distribution between main and nose landing gear depends on the center of gravity position. To have good control characteristics on ground and to lift the nose at take-off easily, the nose gear static load ratio have to be between 5 % and 20 % as proposed by Raymer [42]. The nose static load factor has been derived from equilibrium of forces and moments and is given in Eq. (7).

$$\frac{F_{NG}}{m g} = \frac{1}{1 + \frac{x_{CG} - x_{NG}}{x_{MG} - x_{CG}}} \quad (7)$$

Aircraft must be prevented from tipping on their tail and overturning during fast cornering for the full range of center of gravity positions. For the calculation of the tipback and overturn angle the formulas given in Eq. (8) have been used. In Fig. 9 the definitions of these angles are shown.

$$\tau_{TB} = \arctan \left( \frac{x_{MG} - x_{CG}}{z_{CG}} \right) \quad (8)$$

$$\tau_{OT} = \arctan \left( \frac{z_{CG}}{\Delta s} \right) \quad \text{with} \quad \Delta s = (x_{CG} - x_{NG}) \sin \left( \arctan \left( \frac{y_{MG}}{x_{MG} - x_{NG}} \right) \right)$$

The limits for the tipback and overturn angle are transferred from the textbook by Raymer [42] and summarized in Table 8. Thereby, the upper limit of the overturn angle equals a lateral acceleration of 0.5g during cornering.

In Fig. 9 further geometrical constraints for the landing gear integration are shown. For each aircraft category the outer main gear wheel span has to be within the given limits. Furthermore, the geometrical constraints for nose down engine clearance  $h_{NDEC}$ , touch down tail clearance  $h_{TC}$ , and engine and wing clearances  $h_{EC}$ ,  $h_{WC}$  for a bank angle of  $\varphi = 5^\circ$  have to be fulfilled. The selected values are given in Table 8.

The introduced landing gear integration consists of a design loop for automatic positioning. Thereby, the main gear wing attachment point is shifted from inboard to outboard position and from front to rear position for each span location. All geometrical constraints are checked for each prescribed position, until a feasible design is found.

In Table 8 the introduced design parameters and constraints are summarized. The design parameters include wing planform and wing section parameters. In addition, the percentage ply share in 10 % steps of the skins, spars, and ribs have been used as design parameters for the more flexible wing optimization. For the conventional composite wing structure of the baseline configuration a fixed standard ply share has been used.

The constraints consist of mass constraints, propulsion constraints, geometrical constraints for airport conformity, landing gear and control surface integration constraints, flight mission constraints, and structural sizing constraints. In Table 8 the used values and there limits are given.

<b>Design parameters</b>	Wing area	$S$
	Aspect ratio	$A$
	Leading edge sweep angle	$\varphi_{LE}$
	Taper ratio inboard	$\lambda_{5/2}$
	Taper ratio mid wing	$\lambda_{9/5}$
	Taper ratio outboard	$\lambda_{14/9}$
	Twist distribution	$\varepsilon_1, \varepsilon_5, \varepsilon_8, \varepsilon_9, \varepsilon_{15}$
	Relative thickness distribution	$(t/c)_1, (t/c)_5, (t/c)_9, (t/c)_{14}$
	Inboard rear spar position	$x_{RS}/c$
	Percentage ply share of skins, spars, and ribs	$(PS_{0^\circ,skin})_i, (PS_{0^\circ,spare})_j, (PS_{0^\circ,rib})_k$
<b>Constraints</b>	Maximum take-off mass	$m_{MTO} = 245\,000\text{ kg}$
	Maximum payload	$m_{P,max} = 48\,000\text{ kg}$
	Residual mass ratio	$m_{Res}/m_{MTO} = 0.3763$
	Specific mass of leading edge high lift device	$m_{LE}/S_{LE} = 30\text{ kg/m}^2$
	Specific mass of trailing edge high lift device	$m_{TE}/S_{TE} = 50\text{ kg/m}^2$
	Thrust specific fuel consumption	$TSFC = \frac{0.245\text{ h}^{-1} + 0.415\text{ h}^{-1} Ma}{g} \sqrt{\frac{\Theta}{\Theta_{SL}}}$
	Wingspan (FAA Group V/ICAO Code E)	$52\text{ m} \leq b \leq 65\text{ m}$
	Rib spacing	$\Delta s_{Ri} = 0.75\text{ m}$
	Fuel tank volume	$V_F \geq V_{F,req}$
	Outer main gear wheel span (ICAO Code E)	$9\text{ m} \leq 2 y_{MG} \leq 14\text{ m}$
	Nose gear static load ratio	$5\% \leq F_{NG}/m g \leq 20\%$
	Tip back angle	$\tau_{tb} \geq 15^\circ$
	Overturn angle	$\tau_{ot} \leq 63^\circ$
	Take-off rotation angle	$\alpha_{TO} \leq 9^\circ$
	Clearance of tail, engine, and wing	$h_{TC}, h_{EC}, h_{WC} \geq 0.4\text{ m}$
	Nose down engine clearance	$h_{NDEC} \geq 0.2\text{ m}$
	Relative x-position of main gear wheel on ground	$x_{MG}/c_{MAC} = 0.6$
	Castor angle of main gear leg	$80^\circ \leq \tau_{Cas} \leq 90^\circ$
	Distance between main gear and center wing box	$2.0\text{ m} \leq \Delta s_{MG/CWB} \leq 2.4\text{ m}$
	Distance between main gear and symmetry plane	$1.4\text{ m} \leq \Delta s_{MG/Sym} \leq 1.6\text{ m}$
Distance between main gear and rear spar	$0.6\text{ m} \leq \Delta s_{MG/RS} \leq 1.4\text{ m}$	
Distance between flap and support beam	$\Delta s_{Flap/SB} \geq 0.2\text{ m}$	
Distance between flap and rear spar	$\Delta s_{Flap/RS} \geq 0.065 c_{MAC}$	
Distance between aileron and rear spar	$\Delta s_{Ail/RS} \geq 0.04 c_{MAC}$	

**Table 8 Design parameters and constraints.**

## B. Wing optimization results for conventional composite wing structure with and without MLA

In this section the wing optimization results for the conventional wing structure are presented. The selected global design parameters of the wing optimizations are summarized in Table 9. Based on the Airbus XRF1 reference aircraft geometry, the twist and thickness distribution have been optimized with the result representing the baseline. In the next step the wing planform including the twist and thickness distribution have been optimized. The last optimization additionally includes the active maneuver load alleviation by using the inboard and outboard control surface deflections.

		Twist and thickness optimization (Baseline)	Planform, twist, and thickness optimization	Planform, twist, and thickness optimization with MLA
Wing area	$S$	-	1	1
Aspect ratio	$A$	-	1	1
Taper ratios	$\lambda_{5/2}, \lambda_{9/5}, \lambda_{14/9}$	-	3	3
Leading edge sweep angle	$\varphi_{LE}$	-	1	1
Twist distribution	$\varepsilon_1, \varepsilon_5, \varepsilon_8, \varepsilon_9, \varepsilon_{15}$	5	5	5
Airfoil thickness distribution	$(t/c)_1, (t/c)_5, (t/c)_9, (t/c)_{14}$	4	4	4
Control surface extension	$\Delta(c_F/c)$	-	1	1
Inboard rear spar position	$x_{RS}/c$	-	1	1
Control surface deflections	$\delta_{in,LC1}, \delta_{out,LC1}, \delta_{ail,LC1}$	-	-	3
	$\delta_{in,LC2}, \delta_{out,LC2}, \delta_{ail,LC2}$	-	-	3
Global design parameters	$n_{DP}$	9	17	23

**Table 9** Global design parameters of wing optimizations with conventional composite wing structure.

The resulting wing geometries and the corresponding twist and thickness distributions are shown in Fig. 10. Thereby, the wing planform, the wing box geometry with the spars and ribs, the landing gear including the support beam, and the control surface geometries are presented. The twist distribution for the rigid “jig-shape” and the elastic “flight-shape” are shown for the optimized wings. For the structural interpretation of the results the absolute wing thickness distribution is given. In addition, the relative thickness distribution for the aerodynamic interpretation is presented.

The result of the twist and thickness optimization shows a wing with a significant thin inboard wing section. With the aero-structural wing optimization an optimal trade-off between cruise flight performance and wing mass in terms of combined fuel consumption has been achieved. In Table 10 an overview of all relevant values is given. The high value of the used fuel tank volume for the design mission indicates that the fuel volume constraint is fulfilled, but for flight missions with further extended range an additional fuselage fuel tank will be required. The results of the wing planform optimizations show increased wingspan and reduced taper ratio. This leads to increased cruise flight performance without drawbacks due to wing mass changes.

In Fig. 11 an overview of the aerodynamic results is given for the optimized wings. For each lift distribution the related elliptical lift distribution is shown by a dashed line and the corresponding center of lift is indicated by a grey rectangle as a reference. The elliptical lift distribution is optimum for planar wings in terms of lift induced drag. For the cruise flight condition the result of the twist and thickness optimization shows a nearly elliptical lift distribution. The results of the wing planform optimizations show cruise flight lift distributions with increased inboard loading in comparison to the elliptical lift distribution. The corresponding center of lift is indicated by a black circle. This leads in combination with the relative airfoil thickness to higher values for the isentropic Mach number in the inboard wing region. In the pull up maneuver a significant inboard load shift occurs due to static aeroelastic effects of the backward swept wing [46, 47]. The high aerodynamic loading results in flow separation in the mid wing region as shown in the upper wing friction coefficient distributions of Fig. 11. With the consideration of the active maneuver load alleviation by deflecting the inboard and outboard control surfaces the region of flow separation is reduced. As expected the inboard load shift increases with the usage of the active maneuver load alleviation system.

In Fig. 12 an overview of the structural results is presented. The element thicknesses (sum of skin thickness and stringer height) are shown for the spars, ribs, and covers of the sized wing box. In addition, the results of the structural sizing are given in terms of the “Margin of Safety” (MoS) for the strength and stability criteria. The MoS shows if a design criterion fails or not. It is the ratio of allowed load and current load minus one:

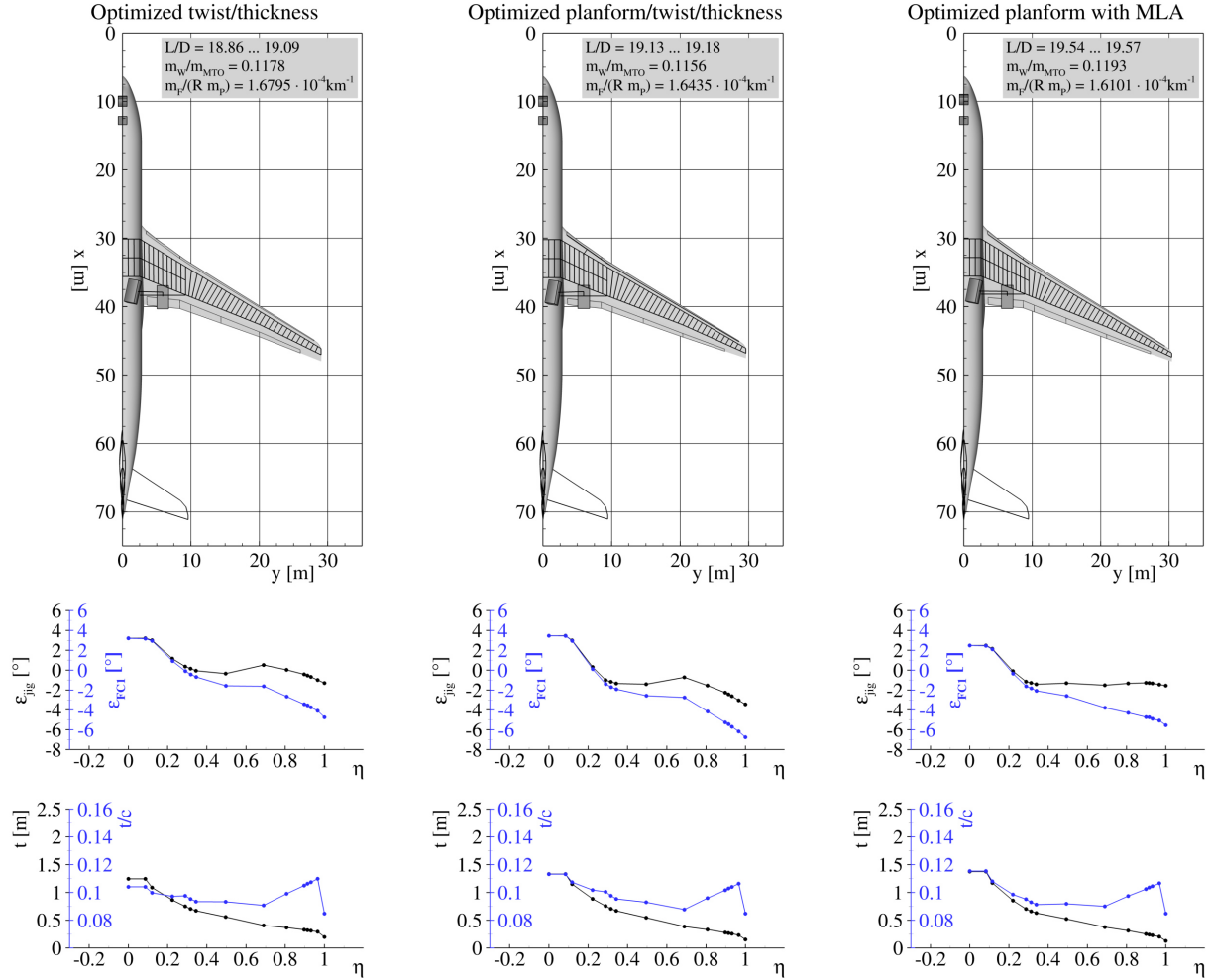


Fig. 10 Geometry overview of wing optimizations with conventional composite wing structure.

$$MoS = \frac{\text{allowed load}}{\text{current load}} - 1 \quad (9)$$

A value lower than zero means the criteria fails. The bigger a positive MoS the bigger is the margin of safety. Different design criteria are applied to ensure a valid structural design. As proposed by Dähne et al. [48] for stiffened panels, the minimum necessary criteria are used with an additional maximum strain criteria:

- Strength for skin and all stringer components,
- Maximum strain criteria for skin and stringer and
- Local and global buckling for skin and all stringer components.

All optimized wings show a similar thickness distribution. The upper and lower covers have the highest and the biggest thicknesses of all components. Therefore, the covers have the biggest mass contribution. All optimization results show a thickness peak at the engine position and the kink. The spars are unstiffened panels and Fig. 12 shows that the spars are sized by stability criteria in all cases. The upper and lower covers are mainly sized by strength criteria for the optimization results without active maneuver load alleviation. The stability criteria are only in very few regions active. In the case with active maneuver load alleviation the reduced load level decreases the dominance of strength criteria.

			Optimized twist and thickness (Baseline)	Optimized planform, twist, and thickness	Optimized planform, twist, and thickness with MLA
<b>Wing Geometry</b>	Wing area	$S_W$	376.2 m <sup>2</sup>	371.1 m <sup>2</sup>	372.0 m <sup>2</sup>
	Wingspan	$b_W$	58.01 m	59.15 m	60.70 m
	Mean aerodynamic chord	$c_{W,MAC}$	7.76 m	7.61 m	7.62 m
	Aspect ratio	$A_W$	8.946	9.428	9.904
	Taper ratio	$\lambda_W$	0.195	0.153	0.128
	Leading edge sweep angle	$\varphi_{W,LE}$	31.9°	31.3°	31.8°
	Flap spar offset	$\Delta s_{Flap/RS}$	0.99 m	1.14 m	0.99 m
	Aileron spar offset	$\Delta s_{Ail/RS}$	0.64 m	0.67 m	0.55 m
Useable fuel tank volume	$V_F$	108.4 m <sup>3</sup>	112.7 m <sup>3</sup>	110.9 m <sup>3</sup>	
<b>Tail geometry</b>	Horizontal tail area	$S_{HTP}$	69.2 m <sup>2</sup>	67.0 m <sup>2</sup>	67.2 m <sup>2</sup>
	Vertical tail area	$S_{VTP}$	49.9 m <sup>2</sup>	50.2 m <sup>2</sup>	51.6 m <sup>2</sup>
<b>Landing Gear</b>	Outer main gear wheel span	$2\gamma_{MG}$	11.74 m	11.86 m	12.66 m
	Nose gear static load factor	$F_{NG}/(m g)$	0.060 . . . 0.084	0.059 . . . 0.083	0.059 . . . 0.083
	Tipback angle	$\tau_{TB}$	18.6° . . . 25.7°	18.3° . . . 25.4°	17.4° . . . 24.1°
	Overturn angle	$\tau_{OT}$	40.6° . . . 40.7°	40.2° . . . 40.3°	40.1° . . . 40.3°
	Tail down angle	$\alpha_{TD}$	11.0°	11.0°	11.6°
	Main gear spar offset	$\Delta s_{MG/RS}$	0.95 m	0.75 m	0.70 m
	Main gear flap offset	$\Delta s_{Flap/SB}$	0.20 m	0.35 m	0.48 m
<b>Masses</b>	Mass of covers	$m_{W,covers}$	14 223 kg	13 898 kg	14 879 kg
	Mass of spars	$m_{W,spars}$	2917 kg	2954 kg	2865 kg
	Mass of ribs	$m_{W,ribs}$	2501 kg	2572 kg	2513 kg
	Wing box mass	$m_{W,box}$	19 640 kg	19 424 kg	20 256 kg
	Wing mass ratio	$m_W/m_{MTO}$	0.1178	0.1156	0.1193
	Operational empty mass ratio	$m_{OE}/m_{MTO}$	0.5199	0.5174	0.5213
<b>Maneuver n=2.5</b>	Lift-to-drag ratio	$L/D$	12.40	12.89	14.26
	Center of pressure	$\gamma_{CoP}/(b/2)$	0.371	0.362	0.332
<b>Study mission</b>	Lift-to-drag ratio	$L/D$	18.86	19.13	19.54
	Center of pressure	$2\gamma_{CoP}/b$	0.420	0.399	0.401
	Fuel consumption	$m_F/(R m_P)$	$1.566 \times 10^{-4} \text{ km}^{-1}$	$1.537 \times 10^{-4} \text{ km}^{-1}$	$1.513 \times 10^{-4} \text{ km}^{-1}$
<b>High speed mission</b>	Lift-to-drag ratio	$L/D$	17.95	18.05	18.67
	Center of pressure	$2\gamma_{CoP}/b$	0.415	0.392	0.394
	Fuel consumption	$m_F/(R m_P)$	$1.631 \times 10^{-4} \text{ km}^{-1}$	$1.616 \times 10^{-4} \text{ km}^{-1}$	$1.570 \times 10^{-4} \text{ km}^{-1}$
<b>Design mission</b>	Payload	$m_P$	33 278 kg	34 185 kg	34 519 kg
	Used fuel tank volume ratio	$V_{F,req}/V_F$	0.973	0.932	0.933
	Lift-to-drag ratio	$L/D$	19.09	19.18	19.57
	Center of pressure	$2\gamma_{CoP}/b$	0.413	0.392	0.393
	Fuel consumption	$m_F/(R m_P)$	$1.923 \times 10^{-4} \text{ km}^{-1}$	$1.865 \times 10^{-4} \text{ km}^{-1}$	$1.819 \times 10^{-4} \text{ km}^{-1}$
<b>Objective</b>	Combined fuel consumption	$m_F/(R m_P)$	$1.680 \times 10^{-4} \text{ km}^{-1}$	$1.644 \times 10^{-4} \text{ km}^{-1}$	$1.610 \times 10^{-4} \text{ km}^{-1}$

**Table 10 Results overview of wing optimizations with conventional composite wing structure.**

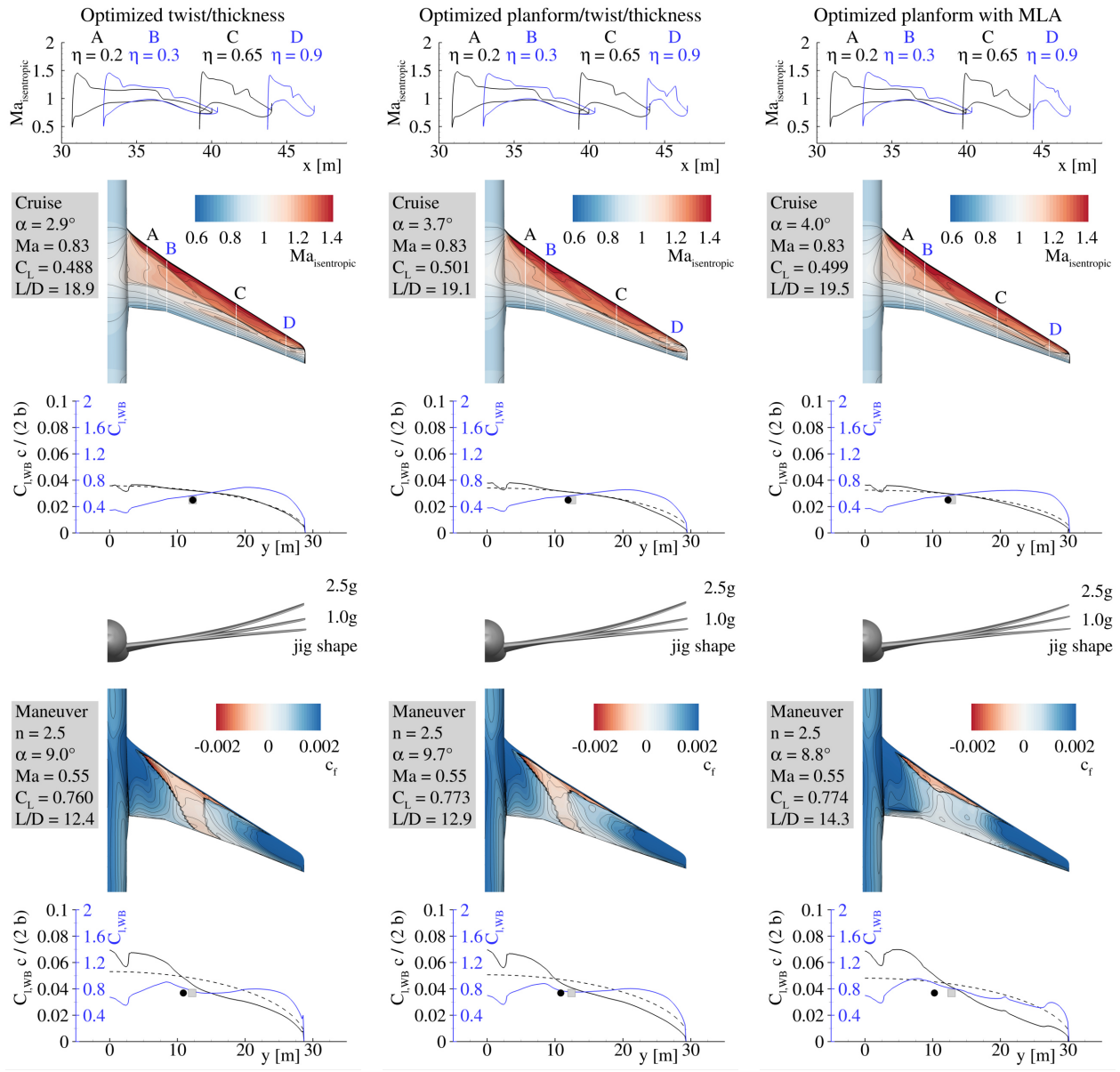


**Fig. 11 Aerodynamic results overview of wing optimizations with conventional composite wing structure.**

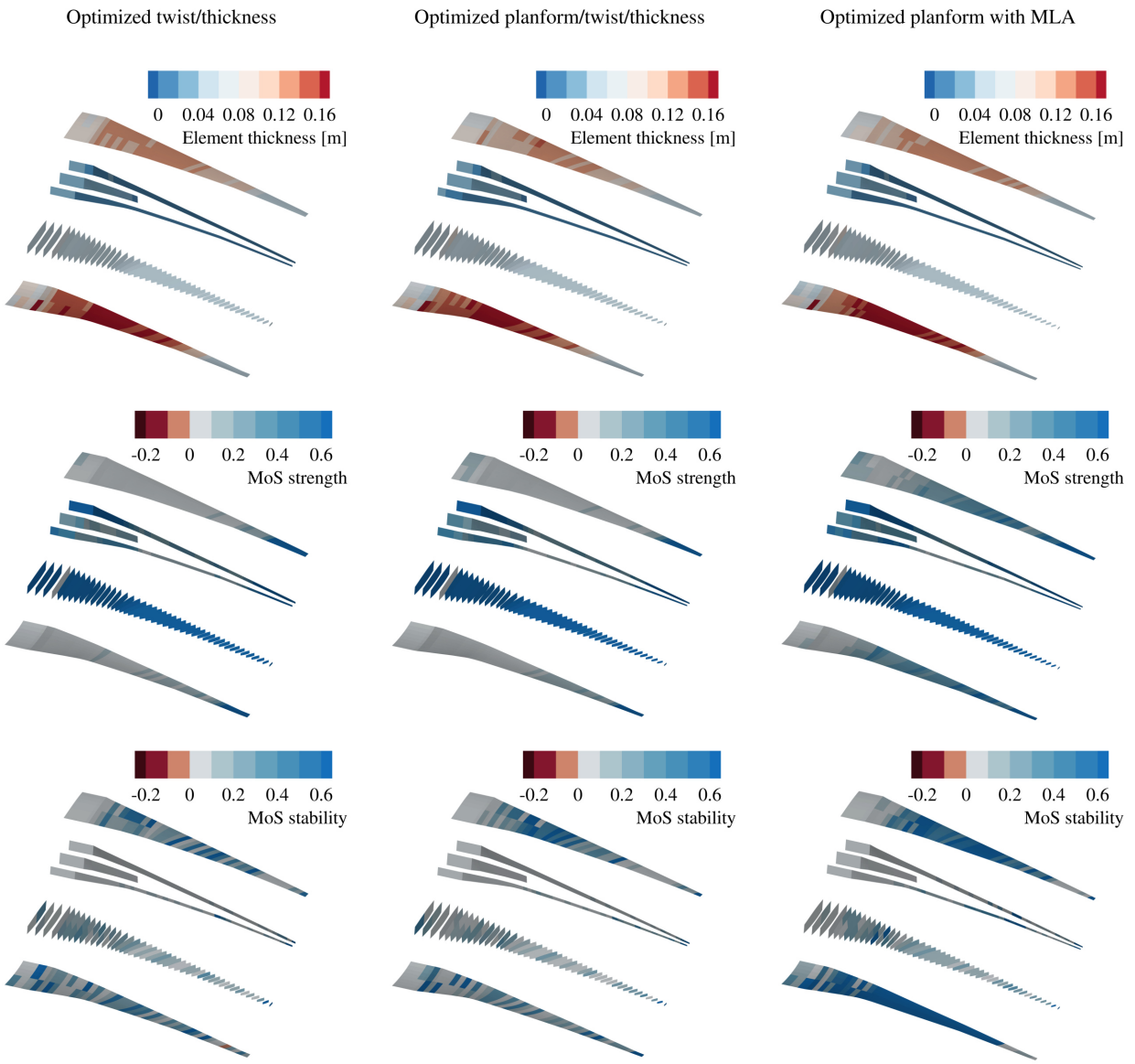


**Fig. 12** Structural results overview of wing optimizations with conventional composite wing structure.

### C. Wing optimization results for more flexible composite wing structure with and without MLA

In this section the wing optimization results for the more flexible composite wing structure are presented. The selected global design parameters of the wing optimizations are summarized in Table 11. Based on the Airbus XRF1 reference aircraft geometry the twist and thickness distribution and the percentage ply share of the lower skin, spars, and ribs have been optimized and the result is representing the baseline with the more flexible wing. In the next optimization the wing planform including the twist and thickness distribution have been optimized. The last optimization additionally includes the active maneuver load alleviation by using the inboard and outboard control surface deflections.

		Baseline optimization with more flexible wing	More flexible wing optimization	More flexible wing optimization with MLA
Wing area	$S$	-	1	1
Aspect ratio	$A$	-	1	1
Taper ratios	$\lambda_{5/2}, \lambda_{9/5}, \lambda_{14/9}$	-	3	3
Leading edge sweep angle	$\varphi_{LE}$	-	1	1
Twist distribution	$\varepsilon_1, \varepsilon_5, \varepsilon_8, \varepsilon_9, \varepsilon_{15}$	5	5	5
Airfoil thickness distribution	$(t/c)_1, (t/c)_5, (t/c)_9, (t/c)_{14}$	2	4	4
Control surface extension	$\Delta(c_F/c)$	-	1	1
Inboard rear spar position	$x_{RS}/c$	-	1	1
Percentage ply share lower skin	$PS_{0^\circ, LS, cen/in/mid/out}$	4	-	-
Percentage ply share spars	$PS_{0^\circ, Sp, cen/in/out}$	3	-	-
Percentage ply share ribs	$PS_{0^\circ, Ri, cen/in/out}$	3	-	-
Control surface deflections	$\delta_{in, LC1}, \delta_{out, LC1}, \delta_{ail, LC1}$	-	-	3
	$\delta_{in, LC2}, \delta_{out, LC2}, \delta_{ail, LC2}$	-	-	3
Global design parameters	$n_{DP}$	17	17	23

**Table 11 Global design parameters for wing optimizations with more flexible wing structure.**

The resulting wing geometries and the corresponding twist and thickness distributions are shown in Fig. 13 for the more flexible wing structure. As a comparison to the results of the wing with the conventional wing structure, the outer shape and inner wing structure are presented for the more flexible wings.

The results show very thin inboard wing sections for all optimized more flexible wings. Based on the significant mass reduction of the more flexible wings the wing aero-structural wing optimizations lead to wings with decreased relative airfoil thicknesses in the inboard wing region. In Table 12 an overview of all relevant values is given. The wing mass of the baseline with more flexible wing has been reduced in the order of 2.5 t in comparison to the twist and thickness optimized wing with conventional wing structure. The results of the wing planform optimizations show increased wingspan and reduced taper ratio here again. This leads to increased cruise flight performance without drawbacks due to wing mass changes. In comparison to the wings with conventional wing structure the optimization results of the more flexible wing show wing geometries with increased wing area, wingspan, and aspect ratio and similar cruise flight performance in terms of lift-to-drag ratios. The corresponding fuel consumptions have been reduced due to lower operational empty masses. Furthermore, the reduced wing stiffness of the more flexible wings results in more inboard center of pressure positions. The used fuel tank volume ratio of the baseline with more flexible wing is on the upper limit for the design mission due to the very thin inboard wing. All optimized wings with the more flexible wing structure fulfill the fuel volume constraint and require an additional fuselage fuel tank for flight missions with further extended range.

An overview of the aerodynamic results is given in Fig. 14 for the optimized wings with more flexible wing structure in comparison to the optimization results of the wings with conventional wing structure. The resulting wing deformations are presented for the cruise flight condition and the 2.5g symmetric pull up maneuver in comparison to the rigid jig-shape. The more flexible wings show higher deflections due to the modified structural concept and the increased strain allowable. The results of the wing planform optimizations show cruise flight lift distributions with increased inboard loading in comparison to the elliptical lift distribution. In the pull up maneuver a significant inboard load shift occurs due to static aeroelastic effects of the backward swept wing. As expected, this inboard load

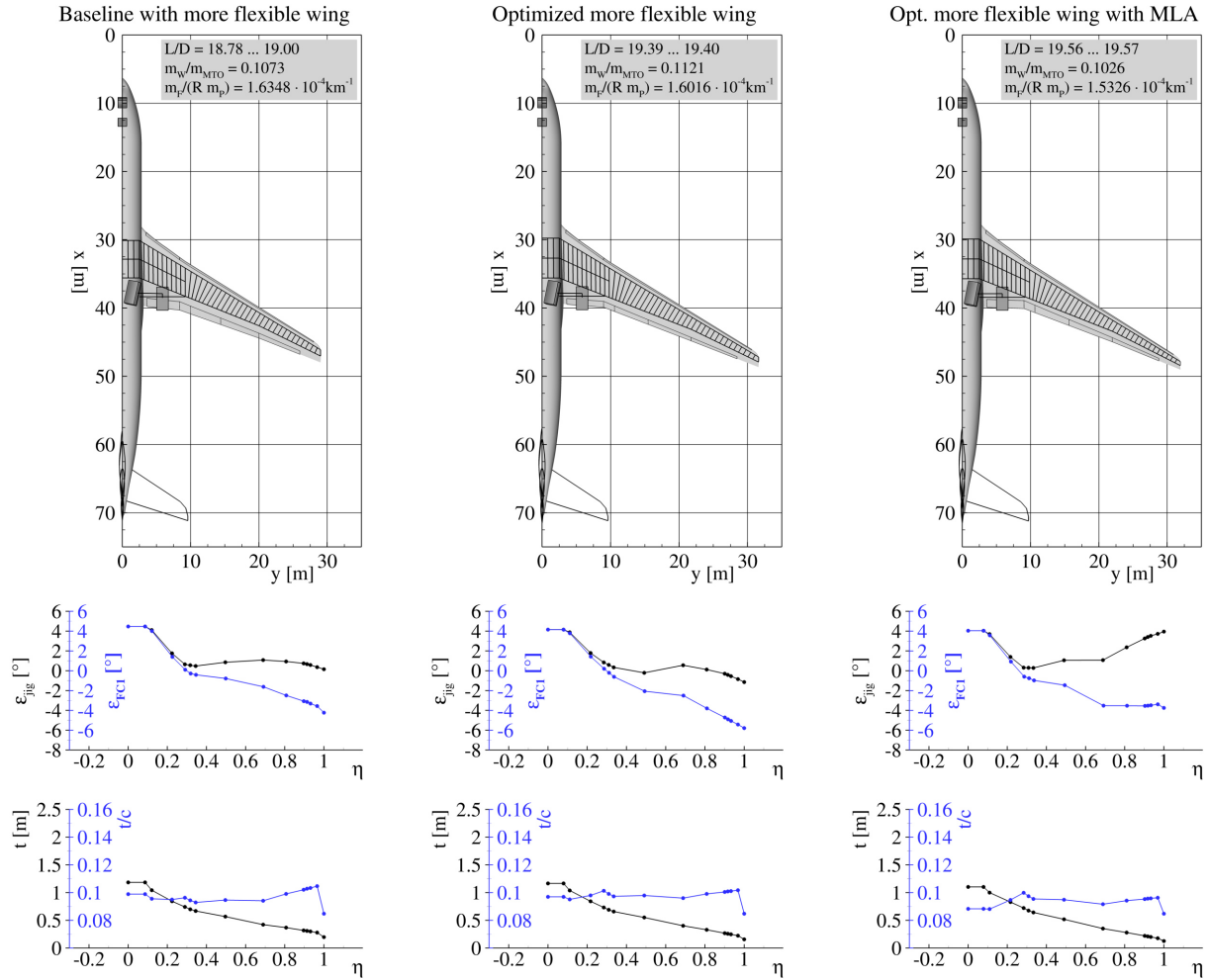


**Fig. 13 Geometry overview of wing optimizations with more flexible wing structure.**

shift of the more flexible wings is stronger in comparison to the optimized wings with conventional wing structure. The high aerodynamic loading results in flow separation in the mid wing region as shown in the upper wing friction coefficient distributions of Fig. 14. With increased wing bending of the wing with optimized planform, the region of flow separation is reduced as well as for the optimized planform including active maneuver load alleviation. As expected the inboard load shift increases with the usage of the active maneuver load alleviation system and reduces the flow separation in the mid wing region significantly. The wing planform optimization of the more flexible wing with active maneuver load alleviation shows a strong reduction of wing bending in the pull up maneuver. Thereby, the inboard load shift is related to a forward shifting of the center of pressure in the case of backward swept wings and the aircraft trimming redistributes the lift between the wing and the horizontal tail. As a result, the lift of the horizontal tail increases and simultaneously the lift of the wing decreases.

In Fig. 15 an overview of the structural results for the more flexible wing structure is presented in analogy to the results for the conventional wing structure. With the increased maximum strain allowable the mass of the upper and lower covers decreases significantly, because the maximum strain criteria is the dominant criteria for the covers on the conventional wing structure. Furthermore, the spars are getting thinner due to the reduced airfoil thickness and the corresponding reduction of buckling areas, where stability is still the sizing criteria for the spars. While optimizing the airfoil thickness the thicknesses of the covers increase slightly with decreasing airfoil thicknesses. By introducing the active maneuver load alleviation, the reduced loads level leads to reduced thicknesses again. The critical MoS for the upper cover is quiet balanced between strength and stability constraints, while the lower cover is still sized by strength.

			Baseline with more flexible wing	Optimized more flexible wing	Optimized more flexible wing with MLA
<b>Wing Geometry</b>	Wing area	$S_W$	376.2 m <sup>2</sup>	387.4 m <sup>2</sup>	384.5 m <sup>2</sup>
	Wingspan	$b_W$	58.01 m	63.20 m	63.79 m
	Mean aerodynamic chord	$c_{W,MAC}$	7.76 m	7.56 m	7.76 m
	Aspect ratio	$A_W$	8.946	10.309	10.582
	Taper ratio	$\lambda_W$	0.195	0.154	0.120
	Leading edge sweep angle	$\varphi_{W,LE}$	31.9°	31.6°	32.3°
	Flap spar offset	$\Delta s_{Flap/RS}$	0.99 m	0.84 m	0.59 m
	Aileron spar offset	$\Delta s_{Ail/RS}$	0.64 m	0.64 m	0.45 m
	Useable fuel tank volume	$V_F$	106.1 m <sup>3</sup>	113.3 m <sup>3</sup>	106.8 m <sup>3</sup>
<b>Tail geometry</b>	Horizontal tail area	$S_{HTP}$	69.2 m <sup>2</sup>	69.4 m <sup>2</sup>	70.7 m <sup>2</sup>
	Vertical tail area	$S_{VTP}$	49.9 m <sup>2</sup>	56.0 m <sup>2</sup>	56.0 m <sup>2</sup>
<b>Landing Gear</b>	Outer main gear wheel span	$2\gamma_{MG}$	11.76 m	11.67 m	11.70 m
	Nose gear static load factor	$F_{NG}/(m g)$	0.060 . . . 0.084	0.059 . . . 0.082	0.060 . . . 0.084
	Tipback angle	$\tau_{TB}$	18.3° . . . 25.4°	17.9° . . . 24.8°	18.5° . . . 25.5°
	Overturn angle	$\tau_{OT}$	41.0° . . . 41.1°	41.1° . . . 41.2°	40.9° . . . 41.1°
	Tail down angle	$\alpha_{TD}$	11.2°	11.2°	11.1°
	Main gear spar offset	$\Delta s_{MG/RS}$	0.95 m	0.95 m	0.85 m
	Main gear flap offset	$\Delta s_{Flap/SB}$	0.21 m	0.32 m	0.31 m
<b>Masses</b>	Mass of covers	$m_{W,covers}$	11 950 kg	13 267 kg	10 995 kg
	Mass of spars	$m_{W,spars}$	2428 kg	2355 kg	2232 kg
	Mass of ribs	$m_{W,ribs}$	2694 kg	2915 kg	3021 kg
	Wing box mass	$m_{W,box}$	17 072 kg	18 537 kg	16 247 kg
	Wing mass ratio	$m_W/m_{MTO}$	0.1073	0.1121	0.1026
	Operational empty mass ratio	$m_{OE}/m_{MTO}$	0.5093	0.5149	0.5056
<b>Maneuver n=2.5</b>	Lift-to-drag ratio	$L/D$	11.51	12.73	12.87
	Center of pressure	$\gamma_{CoP}/(b/2)$	0.365	0.353	0.292
<b>Study mission</b>	Lift-to-drag ratio	$L/D$	18.78	19.40	19.57
	Center of pressure	$2\gamma_{CoP}/b$	0.417	0.387	0.391
	Fuel consumption	$m_F/(R m_P)$	$1.549 \times 10^{-4} \text{ km}^{-1}$	$1.510 \times 10^{-4} \text{ km}^{-1}$	$1.476 \times 10^{-4} \text{ km}^{-1}$
<b>High speed mission</b>	Lift-to-drag ratio	$L/D$	17.66	18.10	18.49
	Center of pressure	$2\gamma_{CoP}/b$	0.412	0.379	0.383
	Fuel consumption	$m_F/(R m_P)$	$1.634 \times 10^{-4} \text{ km}^{-1}$	$1.606 \times 10^{-4} \text{ km}^{-1}$	$1.549 \times 10^{-4} \text{ km}^{-1}$
<b>Design mission</b>	Payload	$m_P$	35 544 kg	35 463 kg	38 304 kg
	Used fuel tank volume ratio	$V_{F,req}/V_F$	0.998	0.920	0.969
	Lift-to-drag ratio	$L/D$	19.00	19.39	19.56
	Center of pressure	$2\gamma_{CoP}/b$	0.409	0.377	0.379
	Fuel consumption	$m_F/(R m_P)$	$1.807 \times 10^{-4} \text{ km}^{-1}$	$1.784 \times 10^{-4} \text{ km}^{-1}$	$1.640 \times 10^{-4} \text{ km}^{-1}$
<b>Objective</b>	Combined fuel consumption	$m_F/(R m_P)$	$1.635 \times 10^{-4} \text{ km}^{-1}$	$1.602 \times 10^{-4} \text{ km}^{-1}$	$1.533 \times 10^{-4} \text{ km}^{-1}$

**Table 12 Results overview of wing optimizations with more flexible wing structure.**

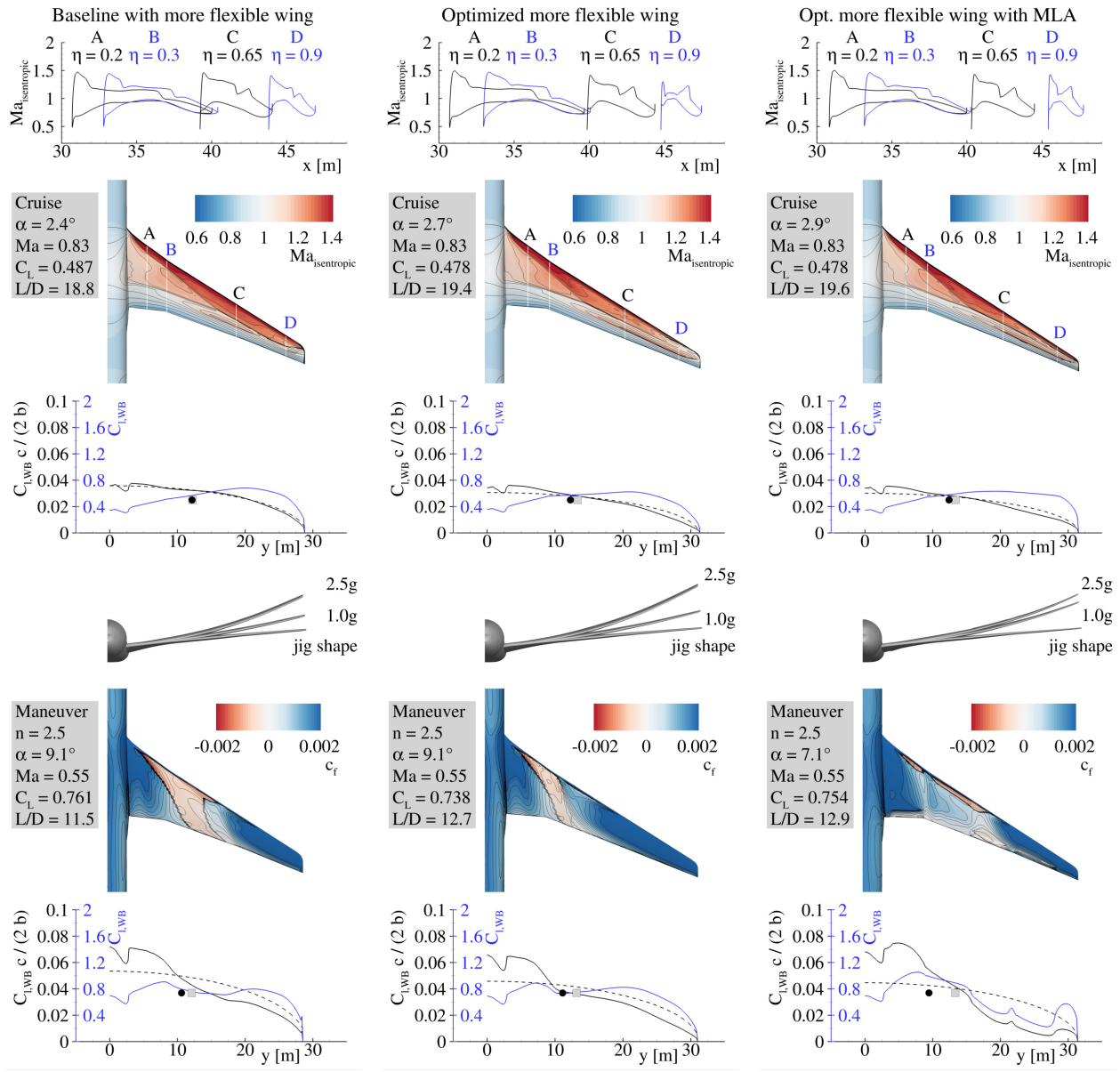
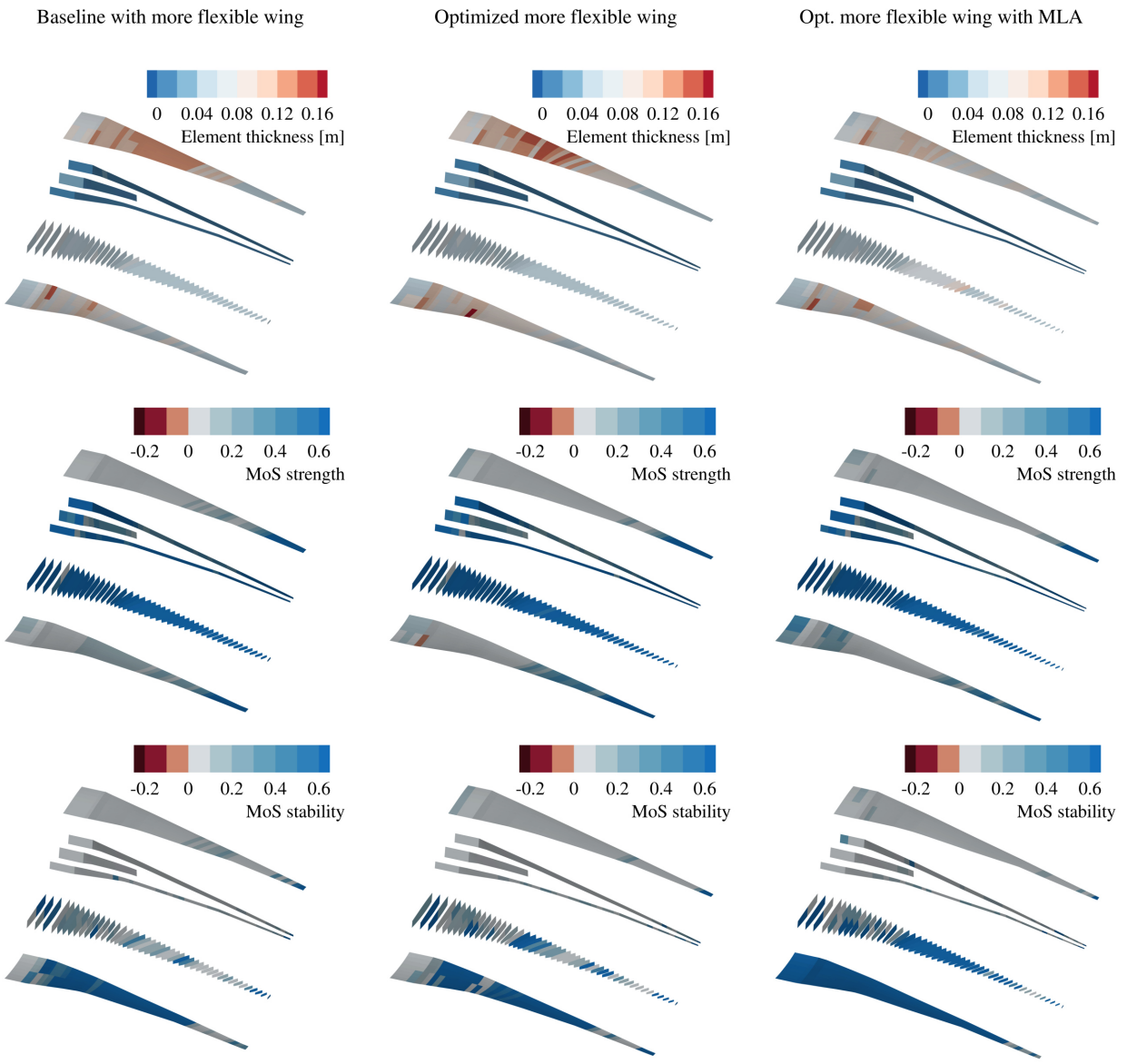


Fig. 14 Aerodynamic results overview of wing optimizations with more flexible wing structure.



**Fig. 15** Structural results overview of wing optimizations with more flexible wing structure.

#### D. Result overview and assessment of the more flexible wing concept

The main results of the aero-structural wing optimizations are summarized in Tab. 13. The values for the combined fuel consumption are presented in the last row and shows the potential of more flexible wings to reduce the  $CO_2$  emissions per passenger kilometer.

Optimization	Reference	Reduction of combined fuel consumption
Baseline with more flexible wing	Optimized twist and thickness (Baseline)	2.7 %
Optimized more flexible wing	Optimized planform, twist, and thickness	2.5 %
Optimized more flexible wing with MLA	Optimized planform, twist, and thickness with MLA	4.8 %
Optimized more flexible wing with MLA	Airbus XRF1 (optimized twist, results not shown)	12.9 %

**Table 13** More flexible wing optimization results overview.

With the introduced more flexible wing concept a reduction of the combined fuel consumption in the order of 3 % has been achieved for the optimizations without the consideration of active maneuver load alleviation. The more flexible wing concept shows for wing optimizations with active maneuver load alleviation an additional reduction of the combined fuel consumption in the order of 2 % due to snowball effects. In comparison to the twist optimized reference aircraft Airbus XRF1, the introduction of the more flexible wing with active maneuver load alleviation technology, leads to reductions of the combined fuel consumption in the order of 13 % after aero-structural wing optimization. The results for the reference aircraft Airbus XRF1 are not presented here, because of restricted publication rules.

In Fig. 16 an overview for the results of the aero-structural wing optimizations is shown. For all aero-structural wing analysis the cruise flight performance, the wing mass ratio, and the corresponding combined fuel consumption are summarized.

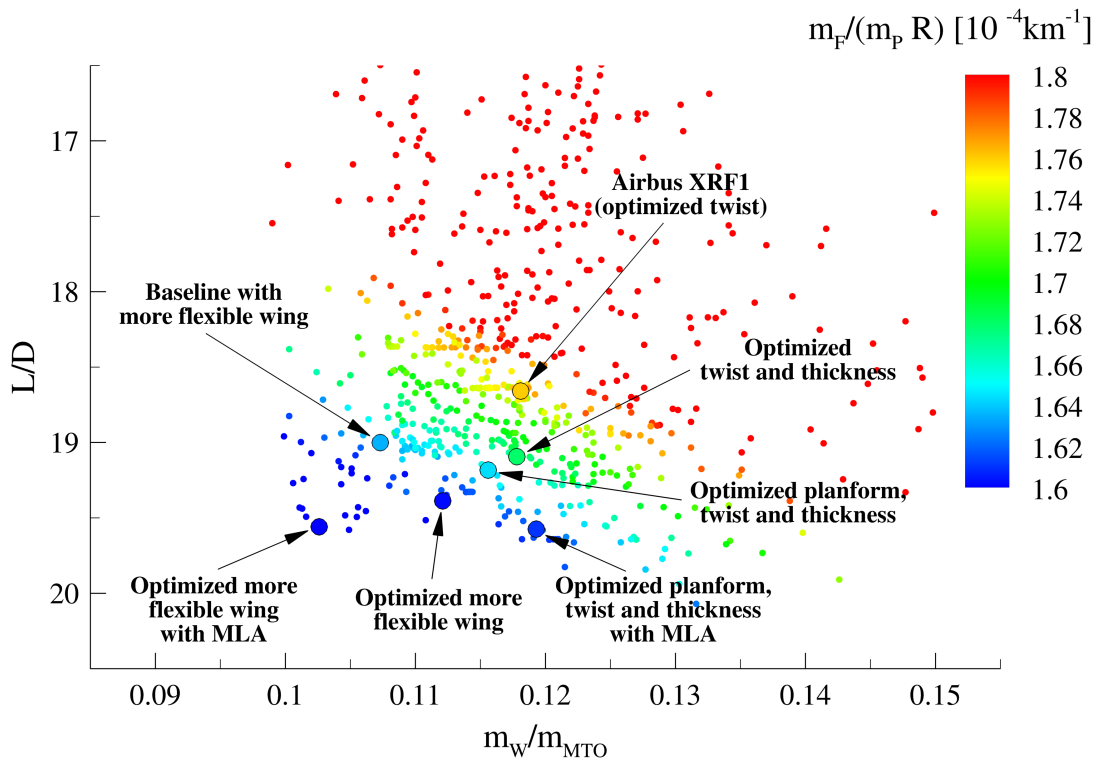


**Fig. 16** Aero-structural wing optimization results overview.

The combined fuel consumption depends on cruise flight performance and wing mass. The global search in the design space shows different combinations of these two counterparts with the same objective function value. However, the global search has been converged with a acceptable accuracy for practical wing optimizations.

### E. Computing time

The aero-structural wing analysis based on high-fidelity methods requires a relatively high computing effort. For the parallel execution of the flow simulations including the volume mesh deformations the HPC-cluster C<sup>2</sup>A<sup>2</sup>S<sup>2</sup>E (Center for Computer Applications in AeroSpace Science and Engineering) of the DLR Institute of Aerodynamics and Flow Technology has been used. In this work the flow simulations use 12 nodes of the C<sup>2</sup>A<sup>2</sup>S<sup>2</sup>E-cluster, which equates to 288 processor cores. All other simulation programs are executed on local workstations.

Process	Simulation program	Program calls	Computing time	Computing time ratio
CAD model update	CATIA® V5	1	2.7 min	2.4 %
Aerodynamic surface mesh generation	Pointwise®	1	0.7 min	0.6 %
Structural model generation	DELiS	1	2.9 min	2.5 %
Flow simulation and volume mesh deformation	FlowSimulator including TAU-Code	5	72.9 min	64.4 %
Structural analysis and sizing process	MSC Nastran™ and HyperSizer®	6	29.8 min	26.3 %
Data transfer	-	-	4.3 min	3.8 %
			113.2 min	100 %

**Table 14** Example of the required computing time of the disciplinary simulation programs for an aero-structural wing analysis.

An example of the required computing time and the corresponding computing time ratio of the disciplinary simulation programs for an aero-structural wing analysis is given in Table 14. In this example 5 fluid-structure coupling iterations have been performed to reach the aeroelastic equilibrium of all considered flight conditions. With approximately 64 %, the parallel execution of the flow simulations including the volume mesh deformations for fluid-structure coupling requires the largest percentage of the computing time. Nevertheless, the computing time for the flow simulation is relatively short for aero-structural coupled simulations based on the Reynolds-averaged Navier–Stokes equations (RANS) due to the high degree of parallelization. The structural analysis and sizing process using the finite element method (FEM) is comparatively efficient. It only needs a percentage of computing time in the order of 30 %.

To summarize, it can be stated that a global aero-structural wing optimization with 17 design parameters requires an overall computing time in the order of 2 weeks.

## V. Conclusion and Outlook

In this work, the assessment of the more flexible wing concept has been successfully demonstrated by using an integrated process for aero-structural wing optimization based on high fidelity simulation methods. The comparison of optimization results with the same objective, design parameters, and constraints allows a proper technology assessment. To find the optimum trade-off between aerodynamic performance and wing mass for the more flexible wing, the twist and thickness distribution and the wing planform design parameters have been involved in the wing optimization. The results of this optimization show the expected reduction of the combined fuel consumption due to an increased aerodynamic performance under cruise flight conditions. This increase in aerodynamic performance has been achieved with higher aspect ratio and reduced taper ratio of the wing.

With the application of more flexible wings, the significance of static aeroelastic effects for the prediction of cruise flight performance and passive maneuver load alleviation has been shown. The structural wing sizing of the modified structural concept, with increased strain allowable, results in a significant wing mass reduction and more wing flexibility. This mass reduction of the more flexible wing can be explained with the increased utilization of the composite material and the passive load alleviation under maneuver flight conditions.

Within the wing planform optimizations only 1 % of the wing geometries in the selected design space have fulfilled the geometrical constraints and have been considered in the aero-structural wing analysis. This observation shows the importance of the consideration of landing gear integration and control surface constraints.

Another aspect of the wing optimization results obtained, is the resulting thin inboard wing, which contradicts conceptual design estimations based on handbook methods and is significantly lower than current aircraft designs. One reason for this is the requested flexibility of airlines for extended range missions, which requires additional fuel tank volume.

In the future, the processes for wing optimization have to be extended with engine design and integration, gust loads prediction, and take-off and landing constraints. Furthermore, the airfoil design has to be integrated with the usage of an airfoil catalog or by gradient based shape optimization. With increasing computational resources and progress in numerical processes, based in high fidelity methods, it is possible for more disciplines and there interactions to be considered in the assessment of new aircraft technologies and configurations.

## Acknowledgments

The authors would like to thank Airbus for providing the XRF1 research test case as opportunity for demonstrating the approaches presented in this publication.

## References

- [1] European Commission, *2008 Addendum to the Strategic Research Agenda*, Office for Official Publications of the European Communities, Luxembourg, Belgium, 2008.
- [2] European Commission, *Flightpath 2050 Europe's Vision for Aviation*, Office for Official Publications of the European Communities, Luxembourg, Belgium, 2011.
- [3] Collier, F., Thomas, R., Burley, C., Nickol, C., Lee, C.-M., and Tong, M., "Environmentally Responsible Aviation-Real Solutions for Environmental Challenges Facing Aviation," *27th Interational Congress of the Aeronautical Sciences, ICAS 2010, Nice, France*, 2010.
- [4] Bezos-O'Connor, G. M., Mangelsdorf, M. F., Maliska, H. A., Washburn, A. E., and Wahls, R. A., "Fuel Efficiencies Through Airframe Improvements," *3rd AIAA Atmospheric Space Environments Conference*, 2011.
- [5] Kenway, G. W. K., and Martins, J. R. R. A., "High-fidelity aerostructural optimization considering buffet onset," *Proceedings of the 16th AIAA/ISSMO Multidisciplinary Analysis and Optimization Conference, Texas, USA*, 2015.
- [6] White, R. J., "Improving the Airplane Efficiency by Use of Wing Maneuver Load Alleviation," *Journal of Aircraft*, Vol. 8, No. 10, 1971, pp. 769–775. doi:10.2514/3.59169.
- [7] Bendixen, G. E., O'Connell, R. F., and Siegert, C. D., "Digital active control system for load alleviation for the Lockheed L-1011," *The Aeronautical Journal*, Vol. 85, No. 849, 1981, pp. 430–436. doi:10.1017/S0001924000030244.
- [8] Jameson, A., Leoviriyakit, K., and Shankaran, S., "Multi-point Aero-Structural Optimization of Wings Including Planform Variations," *45th Aerospace Sciences Meeting and Exhibit, Reno, Nevada, USA*, 2007.
- [9] Martins, J. R. R. A., and Hwang, J. T., "Review and Unification of Methods for Computing Derivatives of Multidisciplinary Computational Models," *AIAA Journal*, Vol. 51, 2013, pp. 2582–2599.
- [10] Liem, R. P., Kenway, G. K. W., and Martins, J. R. R. A., "Multimission Aircraft Fuel-Burn Minimization via Multipoint Aerostructural Optimization," *AIAA Journal*, Vol. 53, 2015, pp. 104–122. doi:10.2514/1.J052940.
- [11] Keye, S., Klimmek, T., Abu-Zurayk, M., Schulze, M., and Ilić, Č., "Aero-Structural Optimization of the NASA Common Research Model," *AIAA Aviation and Aeronautics Forum and Exposition (AVIATION)*, 2017.
- [12] Görtz, S., Ilić, Č., Jepsen, J., Leitner, M., Schulze, M., Schuster, A., Scherer, J., Becker, R.-G., Zur, S., and Petsch, M., "Multi-Level MDO of a Long-Range Transport Aircraft Using a Distributed Analysis Framework," *18th AIAA/ISSMO Multidisciplinary Analysis and Optimization Conference, Denver, USA*, 2017. URL <https://elib.dlr.de/112689/>.
- [13] Görtz, S., Krumbein, A., Ritter, M., and Hofmann, J., "DLR-Projekt VicToria - Virtual Aircraft Technology Integration Platform," *Deutscher Luft- und Raumfahrtkongress 2018*, 2018. URL <https://elib.dlr.de/121695/>.
- [14] Wunderlich, T. F., Abu-Zurayk, M., Ilić, Č., Jepsen, J., Schulze, M., Leitner, M., Schuster, A., Dähne, S., Petsch, M., Becker, R.-G., Zur, S., and Gottfried, S., "Overview of collaborative high performance computing-based MDO of transport aircraft in the DLR project VicToria," *Deutscher Luft- und Raumfahrtkongress 2018*, 2018. URL <https://elib.dlr.de/125555/>.

- [15] Wunderlich, T. F., Dähne, S., Heinrich, L., and Reimer, L., “Multidisciplinary optimization of an NLF forward swept wing in combination with aeroelastic tailoring using CFRP,” *CEAS Aeronautical Journal*, Vol. 8, No. 4, 2017, pp. 673–690. doi:10.1007/s13272-017-0266-z, URL <https://doi.org/10.1007/s13272-017-0266-z>.
- [16] Wunderlich, T. F., and Reimer, L., “Integrated Process Chain for Aerostructural Wing Optimization and Application to an NLF Forward Swept Composite Wing,” *AeroStruct: Enable and Learn How to Integrate Flexibility in Design*, Notes on Numerical Fluid Mechanics and Multidisciplinary Design (NNFM), Vol. 138, edited by R. Heinrich, Springer, Cham, 2018, pp. 3–33. doi:[https://doi.org/10.1007/978-3-319-72020-3\\_1](https://doi.org/10.1007/978-3-319-72020-3_1).
- [17] Martins, J. R. R. A., and Lambe, A. B., “Multidisciplinary Design Optimization: A Survey of Architectures,” *AIAA Journal*, Vol. 51, 2013, pp. 2049–2075.
- [18] Lambe, A. B., and Martins, J. R. R. A., “Extensions to the Design Structure Matrix for the Description of Multidisciplinary Design Analysis and Optimization Processes,” *Structural and Multidisciplinary Optimization*, Vol. 46, 2012, pp. 273–284.
- [19] Liersch, C. M., and Hepperle, M., “A distributed toolbox for multidisciplinary preliminary aircraft design,” *CEAS Aeronautical Journal*, Vol. 2, No. 1–4, 2011, pp. 57–68. doi:10.1007/s13272-011-0024-6.
- [20] Nagel, B., Böhnke, D., Gollnick, V., Schmollgruber, P., Rizzi, A., Rocca, G. L., and Alonso, J. J., “Communication in Aircraft Design Can we Establish a Common Language,” *28th Interantional Congress of the Aeronautical Sciences, ICAS 2012*, 2012.
- [21] Rempke, A., “Netzdeformation mit Elastizitätsanalogie in multidisziplinärer FlowSimulator-Umgebung,” *20. DGLR - Fach-Symposium der STAB 2016*, Vol. 2016, 2016, pp. 128–129.
- [22] Meinel, M., and Einarsson, G. O., “The FlowSimulator framework for massively parallel CFD applications,” *PARA 2010 conference, 6-9 June, Reykjavik, Iceland*, 2010.
- [23] Reimer, L., Vollmer, D., Einarsson, G. O., Görtz, S., Gerhold, T., Heinrich, R., Kroll, N., Michler, A., Ritter, M., Neumann, J., and Hansen, L.-U., “Multidisciplinary Analysis Workflow with the FlowSimulator,” *Proceedings of the Onera Scientific Day 2012—CFD Workflow: Mesh, Solving, Visualizing, ...*, Vol. 19, edited by C. Benoit, P. d’Anfray, and T. H. Lê, Amphithéâtre Becquerel, École Polytechnique, Palaiseau, 2012, pp. 23–30. URL <http://www.association-aristote.fr/Fichiers-2012/2012-10-actes.pdf>.
- [24] Reimer, L., Heinrich, R., and Ritter, M., “Towards Higher-Precision Maneuver and Gust Loads Computations of Aircraft: Status of Related Features in the CFD-Based Multidisciplinary Simulation Environment FlowSimulator,” *New Results in Numerical and Experimental Fluid Mechanics XII*, edited by A. Dillmann, G. Heller, E. Krämer, C. Wagner, C. Tropea, and S. Jakirlić, Springer International Publishing, Cham, 2020, pp. 597–607.
- [25] Führer, T., Willberg, C., Freund, S., and Heinecke, F., “Automated model generation and sizing of aircraft structures,” *Aircraft Engineering and Aerospace Technology*, Vol. 88, No. 2, 2016, pp. 268–276. URL <https://elib.dlr.de/103351/>.
- [26] Siggel, M., Kleinert, J., Stollenwerk, T., and Maierl, R., “TiGL: An Open Source Computational Geometry Library for Parametric Aircraft Design,” *Mathematics in Computer Science*, Vol. 13, 2019, pp. 367–389. URL <https://elib.dlr.de/124524/>.
- [27] Geuzaine, C., and Remacle, J.-F., “Gmsh: A 3-D finite element mesh generator with built-in pre- and post-processing facilities,” *International Journal for Numerical Methods in Engineering*, Vol. 79, No. 11, 2009, pp. 1309–1331. doi:10.1002/nme.2579, URL <https://onlinelibrary.wiley.com/doi/abs/10.1002/nme.2579>.
- [28] Kamakoti, R., and Shyy, W., “Fluid-structure interaction for aeroelastic applications,” *Progress in Aerospace Sciences*, Vol. 40, No. 8, 2005, pp. 535–558.
- [29] Lam, X. B., S.Kim, Y., Hoang, A. D., and Park, C. W., “Coupled Aerostructural Design Optimization Using the Kriging Model and Integrated Multiobjective Optimization Algorithm,” *Journal of Optimization Theory and Applications*, Vol. 142, No. 3, 2009, pp. 533–556.
- [30] Gerhold, T., “Overview of the Hybrid RANS TAU-Code, In: Kroll N., Fassbender J. (Eds) MEGAFLOW - Numerical Flow Simulation Tool for Transport Aircraft Design,” *Notes on Multidisciplinary Design*, Vol. 89, 2005.
- [31] Schwamborn, D., Gerhold, T., and Heinrich, R., “The DLR TAU-Code: Recent Applications in Research and Industry,” *European Conference on Computational Fluid Dynamics, ECCOMAS CFD 2006 Conference, Delft, The Netherlands*, 2006.
- [32] Tinoco, E. N., Brodersen, O. P., Keye, S., Laffin, K. R., Feltrop, E., Vassberg, J. C., Mani, M., Rider, B., Wahls, R. A., Morrison, J. H., Hue, D., Roy, C. J., Mavriplis, D. J., and Murayama, M., “Summary Data from the Sixth AIAA CFD Drag Prediction Workshop: CRM Cases,” *Journal of Aircraft*, Vol. 55, No. 4, 2018, pp. 1352–1379.

- [33] Barnewitz, H., and Stickan, B., “Improved Mesh Deformation,” *Notes on Numerical Fluid Mechanics and Multidisciplinary Design*, Vol. 122, edited by B. Eisfeld, H. Barnewitz, W. Fritz, and F. Thiele, 2013, pp. 219–243. doi:10.1007/978-3-642-36185-2\_9.
- [34] Wilke, G. A., “Variable-Fidelity Methodology for the Aerodynamic Optimization of Helicopter Rotors,” *AIAA Journal*, 2019, pp. 1–14. doi:https://doi.org/10.2514/1.J056486.
- [35] Jones, D. R., Schonlau, M., and Welch, W. J., “Efficient Global Optimization of Expensive Black-Box Functions,” *Journal of Global Optimization*, Vol. 13, 1998, pp. 455–492.
- [36] Forrester, A., Sobester, A., and Keane, A., *Engineering Design via Surrogate Modelling: A Practical Guide*, Wiley, 2008.
- [37] Krige, D. G., “A Statistical Approach to Some Basic Mine Valuation Problems on the Witwatersrand,” *Journal of the Chemical, Metallurgical and Mining Society of South Africa*, Vol. 52, No. 6, 1951, pp. 119–139. doi:10.2307/3006914, URL <http://dx.doi.org/10.2307/3006914>.
- [38] Military, M.-H.-F., *Composite Materials Handbook, Polymer Matrix Composites: Materials Usage, Design, and Analysis*, Vol. 3 of 5, US Department of Defense, 2002.
- [39] Bach, T., and Hühne, C., “Structural Optimization of Stiffened Composite Panels for Highly Flexible Aircraft Wings,” *12th World Congress of Structural and Multidisciplinary Optimization (WCSMO), Braunschweig, Germany*, edited by A. Schumacher, T. Vietor, S. Fiebig, K.-U. Bletzinger, and K. Maute, Springer, Cham, 2018, pp. 838–849. doi:https://doi.org/10.1007/978-3-319-67988-4.
- [40] LTH-Arbeitskreise, *Luftfahrttechnisches Handbuch*, IABG LTH-Koordinierungsstelle, Ottobrunn, 2008.
- [41] Roskam, J., *Airplane Design Part 1: Preliminary Sizing of Airplanes*, Design, Analysis and Research Corporation, 120 East Ninth Street, Suite 2, Lawrence, Kansas, 66044, USA, Lawrence, Kansas, USA, 1989.
- [42] Raymer, D. P., *Aircraft Design: A Conceptual Approach*, third edition ed., American Institute of Aeronautics and Astronautics, 1999.
- [43] Jenkinson, L. R., Simpkin, P., and Rhodes, D., *Civil Jet Aircraft Design*, AIAA education series, American Institute of Aeronautics and Astronautics (AIAA), 1999.
- [44] Mattingly, J. D., Heiser, W. H., and Pratt, D. T., *Aircraft Engine Design*, second edition ed., American Institute of Aeronautics and Astronautics, 2002.
- [45] Nicolai, L. M., and Carichner, G., *Fundamentals of Aircraft and Airship Design*, AIAA education series, Vol. 1, American Institute of Aeronautics and Astronautics, 2010.
- [46] Wunderlich, T. F., “Multidisziplinäre Optimierung von Flügeln für Verkehrsflugzeuge mit Berücksichtigung der statischen Aeroelastizität,” Ph.D. thesis, Technische Universität Braunschweig, 3 2013.
- [47] Wunderlich, T. F., “Multidisciplinary wing optimization of commercial aircraft with consideration of static aeroelasticity,” *CEAS Aeronautical Journal*, Vol. 6, No. 3, 2015, pp. 407–427. doi:10.1007/s13272-015-0151-6.
- [48] Dähne, S., Bach, T., and Hühne, C., “Steps to Feasibility for Laminar Wing Design in a Multidisciplinary Environment,” *29th Congress of the International Council of the Aeronautical Sciences, ICAS 2014*, 2014.